nature cardiovascular research

Article

https://doi.org/10.1038/s44161-026-00898-0

Comprehensive m^{6}A landscape from direct RNA sequencing reveals *SYNPO2L* RNA isoform regulation mechanisms in heart failure

Received: 30 October 2025

Accepted: 24 September 2026

Published online: 5 November 2026

Check for updates

Zhihan Xu[1], Chi Tian[2], Jun Wei Chan[3,4], Wikie Tew[1], Galvin L. Q. Tang[1], Rujie Qi[1], Zheyi Tao[1], Daniel G. R. Yim[1], Liang Cui[5], Danh Anh Tuan Luu[1], Junedh M. Amrute[6,7], Vinay Tergaonkar[3,8,9,10], Chang Jie Mick Lee[1] & Roger S. Y. Foo[1,3]

Accumulating evidence suggests that epitranscriptomic regulation, particularly the m^{6}A modification, contributes to heart failure progression. However, modification dynamics are not yet mapped and studied at base resolution and transcript isoform level. Here we use Nanopore direct RNA sequencing to profile m^{6}A remodeling at transcriptome-wide and site-specific resolution in a mouse heart failure model. We identify thousands of differentially methylated sites with distinct sequence motifs and associations with RNA regulatory and cardiac function processes. Cross-species comparison reveals conserved m^{6}A regulatory features in mouse and human heart failure. Isoform-resolved analysis further uncovers co/posttranscriptional regulation events involving isoform switching and m^{6}A regulation in the *SYNPO2L* transcript. Mechanistically, m^{6}A modification, alternative promoter usage and associated regulatory elements collectively explain this observation. Overall, our study provides a comprehensive, high-resolution characterization of m^{6}A landscape and its remodeling in heart failure. Isoform-level regulation exemplifies an underap preciated shaping of RNA expression and modification.

Heart failure is a clinical syndrome characterized by structural and functional cardiac abnormalities, elevated natriuretic peptide levels and cardiogenic pulmonary or systemic congestion[1]. A major underlying cause of heart failure is cardiomyopathy, where alteration of the structure and function of the cardiac muscle contributes to systolic or diastolic dysfunction and consequent disease progression in the absence of timely and appropriate intervention[2,3]. Transverse aortic constriction (TAC) is a widely used mouse model of pressure overload-mediated heart failure in preclinical research[4,5]. TAC with varying degrees of aortic constriction is reported to simulate cardiac phenotypes of varying severities, as assessed by echocardiography and physiological parameters, allowing the recapitulation of different stages of heart failure progression[6].

Transcriptomic regulation is well recognized to underlie the progression of heart failure, including the reactivation of fetal gene isoforms, altered expression of energy metabolism genes and upregulation of inflammatory and fibrotic genes, most of which compensate initially for cardiac stress but ultimately lead to adverse remodeling and functional decline[7,8]. By contrast, the role of epitranscriptomic regulation in heart failure only gained attention in recent years[9].

A full list of affiliations appears at the end of the paper. e-mail: roger.foo@nus.edu.sg

Epitranscriptomics refer to the collection of chemical modifications on RNA molecules that regulate splicing, stability, localization, and translation[10,11]. Among these, N^6-methyladenosine (m^6A) is the most extensively studied in cardiac biology. Key regulators, including the writer Methyltransferase-like 3 (METTL3) and the eraser Fat Mass and Obesity-Associated Protein (FTO), play critical roles in modulating cardiac function[12,13]. During heart failure, m^6A is implicated as both a potential biomarker and a contributor to cardiac remodeling and homeostasis[14–16].

m^6A is predominantly installed within the consensus sequence 5′-DRACH-3′, where the central adenosine is the methylation target[10,17]. MeRIP-seq (m^6A RNA immunoprecipitation sequencing) relies on antibody-based enrichment of modified RNA fragments and typically identifies m^6A peaks spanning 50–200 nucleotides[10,17]. This semi-quantitative approach lacks base-level resolution, limiting precise site identification and differential modification analysis[18]. Oxford Nanopore Technologies (ONT) direct RNA sequencing (DRS) enables high-throughput sequencing of native, full-length RNA molecules[19,20]. DRS detects electrical current fluctuations as RNA strands pass through a nanopore[20]. These signals can be decoded to identify RNA modifications at single-nucleotide resolution[21]. This level of precision facilitates downstream studies of high-resolution site-specific modifications and allows the discovery of the relationship between RNA modifications and RNA isoform diversity[22,23].

RNA modifications are linked to isoform-specific regulation[24,25]. Alternative splicing, promoter usage and polyadenylation generate isoforms with distinct coding potentials, untranslated regions and regulatory properties[26]. Site-specific differences in m^6A deposition may contribute to differential regulation of transcript variants[27,28]. However, previous studies of the cardiac m^6A landscape relied on short-read sequencing, which limits full-length isoform resolution and assignment of modification signals to specific transcripts[14,15]. The interplay between m^6A modification and RNA isoform dynamics therefore remains incompletely understood.

In this Article, we integrate Nanopore DRS with wet-lab experiments to characterize global m^6A distribution and differentially methylated region (DMR) sites in a mouse heart failure model. Cross-species comparison explores conserved regulatory patterns, while transcript isoform analysis identifies co/posttranscriptional regulation at the isoform level. Our study provides a high-resolution cardiac m^6A profile, offering valuable insights for target identification and therapeutic development in heart failure.

Results

Severity-dependent cardiac phenotypes and transcriptomic remodeling in the TAC-induced heart failure model

Left ventricular structure and systolic and diastolic function were assessed by echocardiography at baseline and 2 and 4 weeks after TAC using 2 different degrees of aortic constriction. At week 4, ejection fraction and fractional shortening were significantly reduced, while left ventricular internal dimension at end-diastole significantly increased in both 27G- and 30G-operated mice compared with sham. Functional decline and chamber dilatation were more pronounced in 30G than 27G mice (Fig. 1a–d). Heart weight-to-body weight (HW/BW) ratios increased significantly in both TAC groups and were 1.6-fold higher in 30G than 27G mice (Fig. 1e). Lung weight-to-body weight (LW/BW) ratios increased significantly only in 30G mice (Fig. 1f), indicating pulmonary congestion in this group.

DRS identified characteristic myocardial stress genes *Nppa*, *Nppb*, *Acta1*, *Myh7* and *Postn* as differentially expressed genes (DEGs) in both TAC groups compared with sham (Fig. 1g,h). The groups shared 145 upregulated and 119 downregulated DEGs (Fig. 1i). However, 30G mice exhibited 1,721 unique DEGs versus 97 in 27G mice, representing a 5.7-fold difference in total DEG counts (Fig. 1j and Supplementary Table 1). The marked increase reflects a more extensive transcriptomic perturbation in the 30G group. Gene Ontology (GO) biological process analysis showed that upregulated unique DEGs in 30G mice were enriched in inflammatory response, blood vessel morphogenesis and extracellular matrix organization; downregulated unique DEGs were enriched in metal ion transport, circulatory system process and fatty acid metabolism (Fig. 1k,l).

Taken together, phenotypic and transcriptomic analyses confirmed the presence of pressure overload-induced heart failure in this model. Comparison between 27G and 30G TAC mice confirmed that 30G induced a more severe heart failure phenotype.

Epitranscriptomic analyses uncover differential m^6A regulation in heart failure

Common messenger RNA modifications were detected and quantified using mass spectrometry (Supplementary Table 2). Among the 13 detectable mRNA modifications, global m^6A levels were significantly elevated (9.0% in 27G and 22.6% in 30G). Other modifications remained largely unchanged or showed inconsistent trends across both TAC groups (Fig. 2a–c). To characterize the expression patterns of key m^6A regulatory enzymes, enzymes involved in m^6A installation (writers) and removal (erasers) were analyzed using DRS, including *Mettl3*, *Mettl14*, *Wtap*, *Mettl16*, *Fto* and *Alkbh5*. In 27G mice, *Fto* was significantly downregulated to 0.83-fold (Fig. 2d). In 30G mice, *Mettl16* was upregulated to 1.16-fold, while *Fto* and *Alkbh5* were downregulated to 0.82- and 0.88-fold, respectively (Fig. 2e). Western blotting for protein expression analysis showed no significant changes in 27G mice, although METTL3 showed an increasing trend with $P = 0.052$ (Fig. 2f,g). In 30G mice, m^6A writers including METTL3 and METTL14 were significantly upregulated by 1.33- and 1.32-fold, respectively. The m^6A eraser ALKBH5 was significantly upregulated by 1.54-fold, while FTO showed a decreasing trend with $P = 0.058$ (Fig. 2h).

Overall, there were changes in m^6A regulatory enzyme abundance, particularly at the protein level, but with discordant patterns between RNA and protein expression.

Global m^6A distribution patterns in the heart

Dorado (v1.0.0) provided random-context and DRACH-context models for m^6A basecalling from ONT DRS. The random-context model yielded more low-confidence calls with probabilities of 0.6–0.7, whereas the DRACH-context model yielded more high-confidence calls above 0.9 (Fig. 3a and Extended Data Fig. 1a). To ensure accuracy and specificity in m^6A identification, we proceeded with the DRACH context model for downstream analysis, and the probability threshold for m^6A calls was set at 0.8, with all calls below this value filtered out.

We validated DRS m^6A annotations using GLORI (glyoxal- and nitrite-mediated deamination of unmethylated adenosines) on the same samples, followed by targeted PCR and Sanger sequencing of *Igf1r* and *Neat1* (Fig. 3b and Extended Data Fig. 1b). Two *Igf1r* sites had average DRS modification ratios of 17% and 50%, with corresponding GLORI A/G ratios of 15% and 50%. Although this approach does not precisely quantify m^6A levels, it permits approximate comparison within a sequencing output. GLORI also validated all tested DRS-identified *Neat1* sites, supporting consistency between the methods.

We calculated average m^6A levels across aligned reads for each DRACH adenosine and classified sites as having a high (>0.4), medium (0.1–0.4) or low (<0.1) level of modification. These categories accounted for approximately 5%, 8% and 87% of sites, respectively (Fig. 3c). Among the different DRACH motifs, the GGACU motif showed the highest probability of being highly modified, followed by GGACA and GAACU (Fig. 3d). In a 7-mer context, UGGACUB and CGGACUK (B = C/G/U, K = G/U) had the highest probabilities (>0.4) of being highly modified sites (Fig. 3e). Motif enrichment analysis of all highly modified sites identified UGGACUG as the most frequent motif, consistent with the probability-based ranking (Fig. 3f).

https://doi.org/10.1038/s44161-026-00898-0

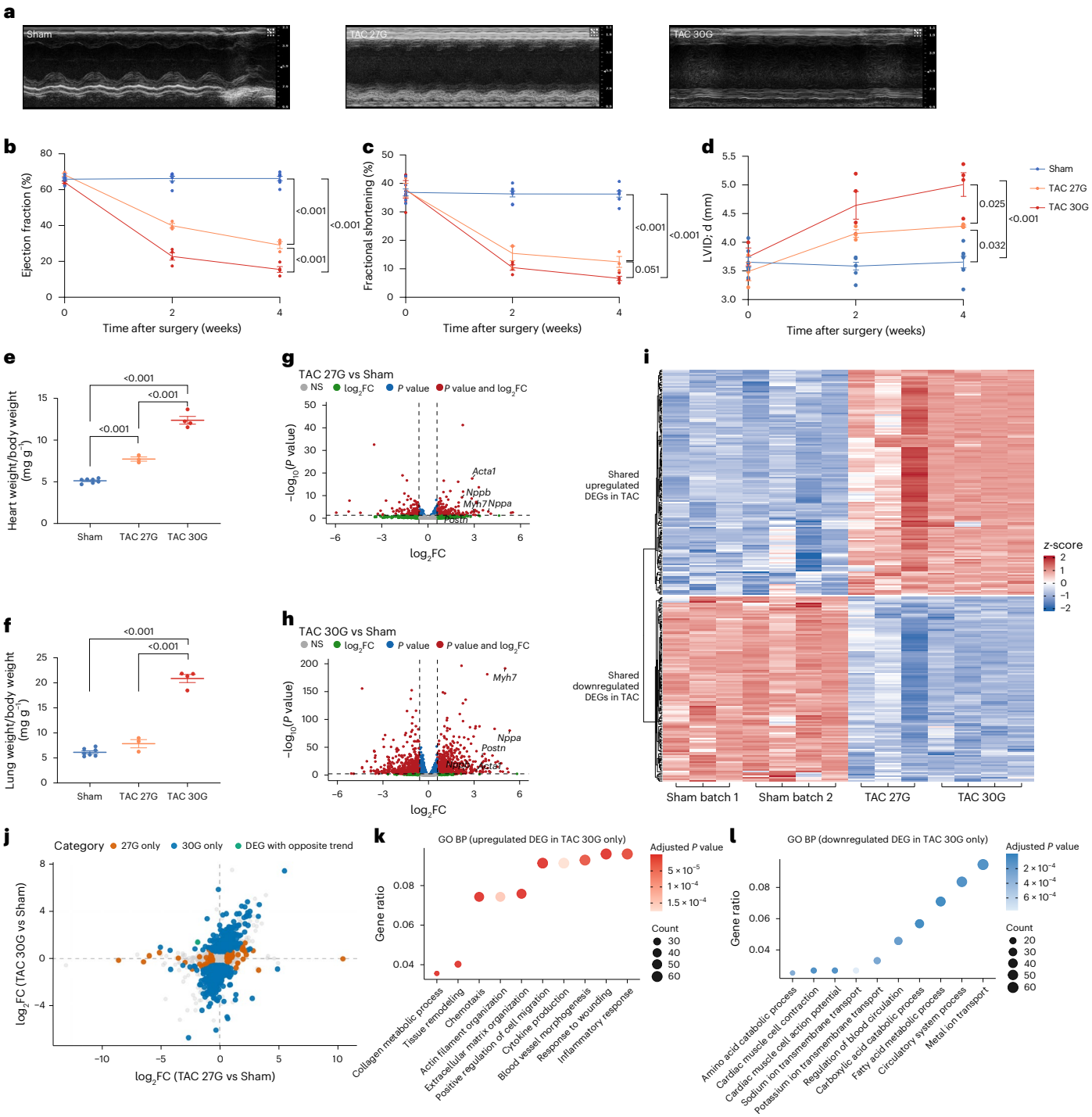


Fig. 1 | Severity-dependent cardiac phenotypes and transcriptomic remodeling in the TAC-induced heart failure model. a, Representative M-mode echocardiography of mice following sham and TAC surgery. **b**–**d**, Measurements of ejection fraction (**b**), fractional shortening (**c**) and left ventricular internal diameters at end-diastole (LVID; d) (**d**) at baseline, 2 weeks and 4 weeks after surgery ($n = 7$ for sham, $n = 3$ for TAC 27G, $n = 4$ for TAC 30G). **e**,**f**, Measurements of heart weight (**e**) and lung weight (**f**), each normalized to body weight at week 4 after surgery ($n = 7$ for sham, $n = 3$ for TAC 27G, $n = 4$ for TAC 30G). **g**,**h**, Volcano plots of gene expression for TAC 27G versus sham ($n = 3$ for each group) (**g**) and TAC 30G versus sham ($n = 4$ for each group) (**h**), with DEGs shown in red ($|\log_2 FC| > 0.58$, adjusted $P < 0.05$). FC, fold change; NS, not significant. **i**, Heat map of shared up- and downregulated DEGs between TAC 27G and 30G mice. **j**, Scatter plot of DEGs unique to either TAC 27G or TAC 30G mice. **k**,**l**, GO biological process analysis of upregulated DEGs (**k**) and downregulated DEGs (**l**) in TAC 30G mice only. Data are shown as mean ± s.e.m. *P* values are annotated to show statistical significance. Statistics was performed using one-way ANOVA with Bonferroni post hoc test in **b**–**f**. Statistical tests for DGE analysis in **g** and **h** and GO enrichment in **k** and **l** are described in Methods, and *P* values were adjusted using the Benjamini–Hochberg procedure.

Base-level m^{6}A annotations for individual transcripts revealed patterns of m^{6}A distribution. For example, in gene *Chrm2* (cholinergic receptor muscarinic 2), m^{6}A sites were enriched in the last exon, extending from the coding sequence to the 3′ untranslated region (3′ UTR) (Fig. 3g). Highly modified m^{6}A sites did not appear in isolation but instead occurred in clusters. Transcriptome-wide nearest-neighbor analysis showed significantly shorter distances between highly modified sites than expected under two null models:

https://doi.org/10.1038/s44161-026-00898-0

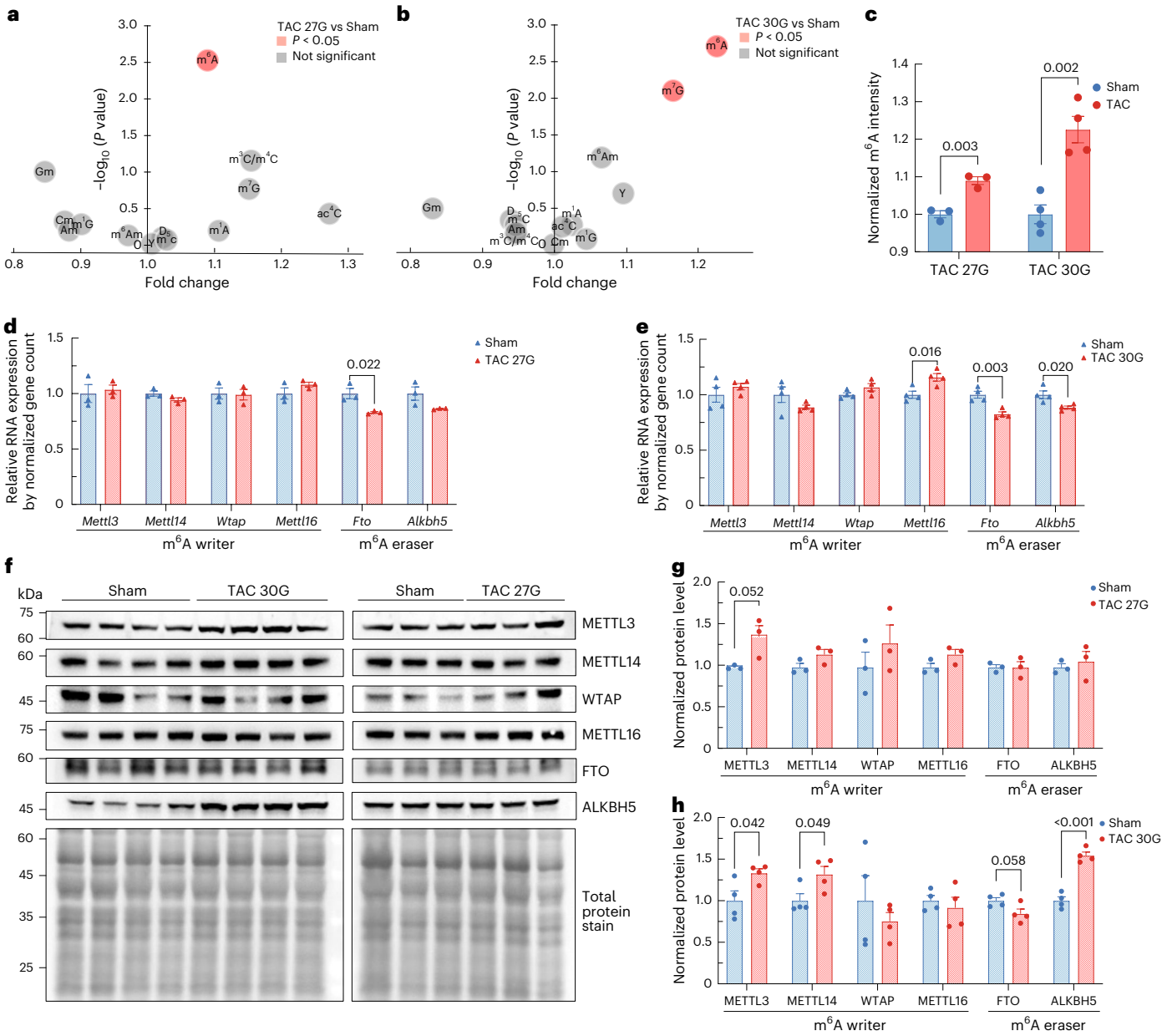


Fig. 2 | Epitranscriptomic analyses uncover differential m^{6}A regulation in heart failure. a,**b**, mRNA modifications in TAC 27G versus sham mice (**a**; $n = 3$ for each group) and TAC 30G versus sham mice (**b**; $n = 4$ for each group), with differentially regulated modifications shown in red ($P < 0.05$). **c**, Normalized m^{6}A modification intensity comparing sham with TAC 27G and TAC 30G mice. **d**,**e**, Relative RNA expression by DRS normalized gene count of common m^{6}A-related enzymes in TAC 27G versus sham (**d**) and TAC 30G versus sham (**e**). **f**, Western blots of METTL3, METTL14, WTAP, METTL16, FTO and ALKBH5 in sham versus TAC 27G (right) and TAC 30G mice (left), with total protein staining as loading control. **g**,**h**, Quantification of protein expression levels comparing sham with TAC 27G (**g**; $n = 3$ for each group) and TAC 30G mice (**h**; $n = 4$ for each group). Data are shown as mean ± s.e.m. *P* values are annotated to show statistical significance. Statistics was performed using unpaired two-tailed Student's *t*-test without adjustment in **a**–**e**, **g** and **h**.

random distribution across transcripts or constrained to GGACU motifs (Fig. 3h), indicating that these sites are nonrandomly distributed and tend to cluster within transcripts. To assess the reported preference of m^{6}A for open RNA regions[29], we predicted minimum free energy (MFE) using ViennaRNA (RNAfold) across 61-nt windows centered on each site[30]. Randomly sampled, equally sized sets of sequences containing sites with a high level of modification had significantly higher MFE than those containing sites with a low level of modification, indicating less stable local structures (Fig. 3i). Together, these findings suggest that highly modified m^{6}A sites tend to cluster within transcripts and preferentially locate at structurally accessible regions.

DMR sites and enriched pathways

DMR analysis between TAC and sham groups identified 698 significantly upregulated and 637 significantly downregulated m^{6}A sites in TAC 27G mice, as well as 1,587 significantly upregulated and 1,169 significantly downregulated m^{6}A sites in TAC 30G mice (Fig. 4a and Supplementary Table 3). In 27G mice, DMR sites were those with median m^{6}A level of ~25% and showed a trend toward an increase after TAC (median, 24.4% to 26.9%, $P = 0.078$) (Fig. 4b). In 30G mice, DMR sites were those with higher median m^{6}A level of ~45% and a significant global increase after TAC (median, 46.3% to 50.8%) (Fig. 4c). Noting differences in the median m^{6}A levels between DMR sites of the two TAC groups, we examined up- and downregulated DMR sites more closely for their

https://doi.org/10.1038/s44161-026-00898-0

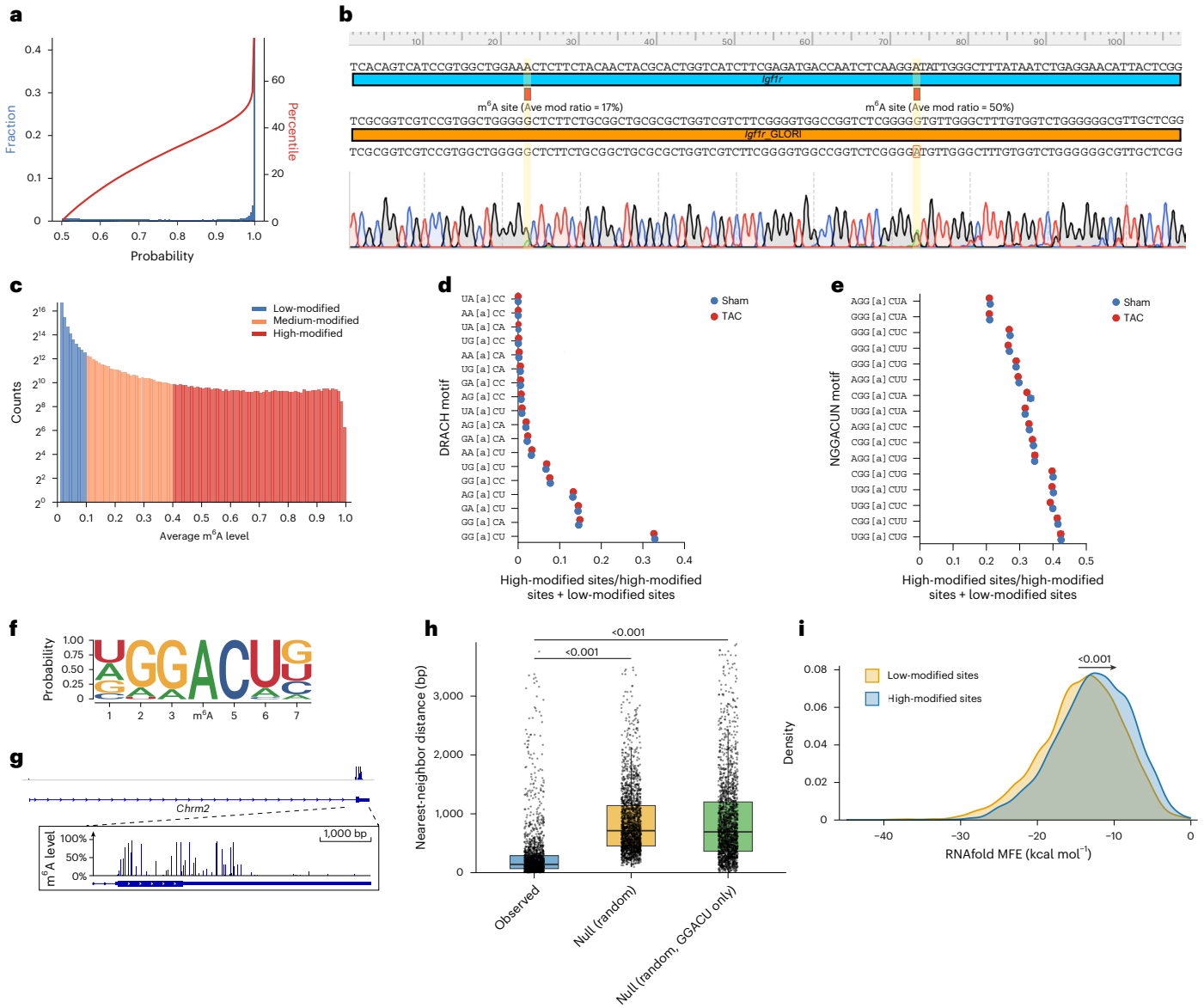


Fig. 3 | Global m^{6}A distribution patterns in the heart. a, Dual-axis plots of base modification probability of m^{6}A calls by DRACH context Dorado m^{6}A basecalling model. Left *y* axis (blue) is the fraction distribution of probability, and right *y* axis (red) is the cumulative percentile of probability. **b**, GLORI detection of m^{6}A sites in transcript *Igf1r*, showing the original sequence (first row), predicted GLORI-treated sequence (second row) and sequencing result with chromatogram (third row), generated with SnapGene software (v8.0.2). Average modification (Ave mod) ratio is calculated as the number of m^{6}A calls divided by the total number of calls at a given site in DRS. **c**, Distribution of average m^{6}A levels at m^{6}A sites categorized as having a high (red), medium (orange) or low (blue) level of modification. **d**,**e**, Probability of m^{6}A sites within different motifs to be highly modified sites in sham and TAC mice, including DRACH motifs (**d**) and NGGACUN motifs (**e**), ($n = 7$ for sham, $n = 7$ for TAC). **f**, Motif enrichment analysis of highly modified sites. **g**, Visualization of m^{6}A level at individual m^{6}A sites in the *Chrm2* transcript using the Integrative Genomics Viewer (v2.19.4)[56]. **h**, Box plot of nearest-neighbor distances between highly modified m^{6}A sites, comparing the observed distribution (blue) to two null models: a random distribution of an equal number of sites across the corresponding transcript (yellow) and a random distribution of an equal number of sites constrained to GGACU motifs on the corresponding transcript (green). Each point represents the transcript-level median distance ($n = 1,859$ for each group). Boxes span the 25th to 75th percentiles, center lines indicate medians and whiskers extend to the most extreme observations within 1.5 times the interquartile range. **i**, Distribution of predicted MFE of RNA secondary structure of sites with high (blue) and low levels of modification (yellow) ($n = 5,000$ for each group). All samples are used for data analysis and plot generation unless otherwise specified. Data are shown as mean ± s.e.m. *P* values are annotated to show statistical significance. Statistics was performed using unpaired two-tailed Student's *t*-test in **d** and **e**, paired one-sided Wilcoxon signed-rank test in **h**, and two-sided Wilcoxon rank-sum test in **i**.

baseline (sham) m^{6}A levels. For 27G mice, upregulated DMR sites were enriched at sites with significantly lower baseline m^{6}A levels with differences exceeding 10%, beyond the expected range defined by the DMR effect size threshold, in contrast to other comparisons (Fig. 4d).

Methylation changes at individual DMR sites showed no global correlation with corresponding gene expression changes in either TAC group (Fig. 4e,f). To assess coordinated transcript-level regulation, we assigned transcripts containing ≥2 DMR sites a direction score, defined as the fraction of upregulated sites (Fig. 4g). All DMR sites changed in the same direction in 66% and 63% of transcripts in TAC 27G and 30G groups, respectively, while the remaining ~35% showed mixed regulation. We defined differentially methylated transcripts as those containing at least two consistently regulated DMR sites. Restricting the analysis to these transcripts, we found that the majority did not show

https://doi.org/10.1038/s44161-026-00898-0

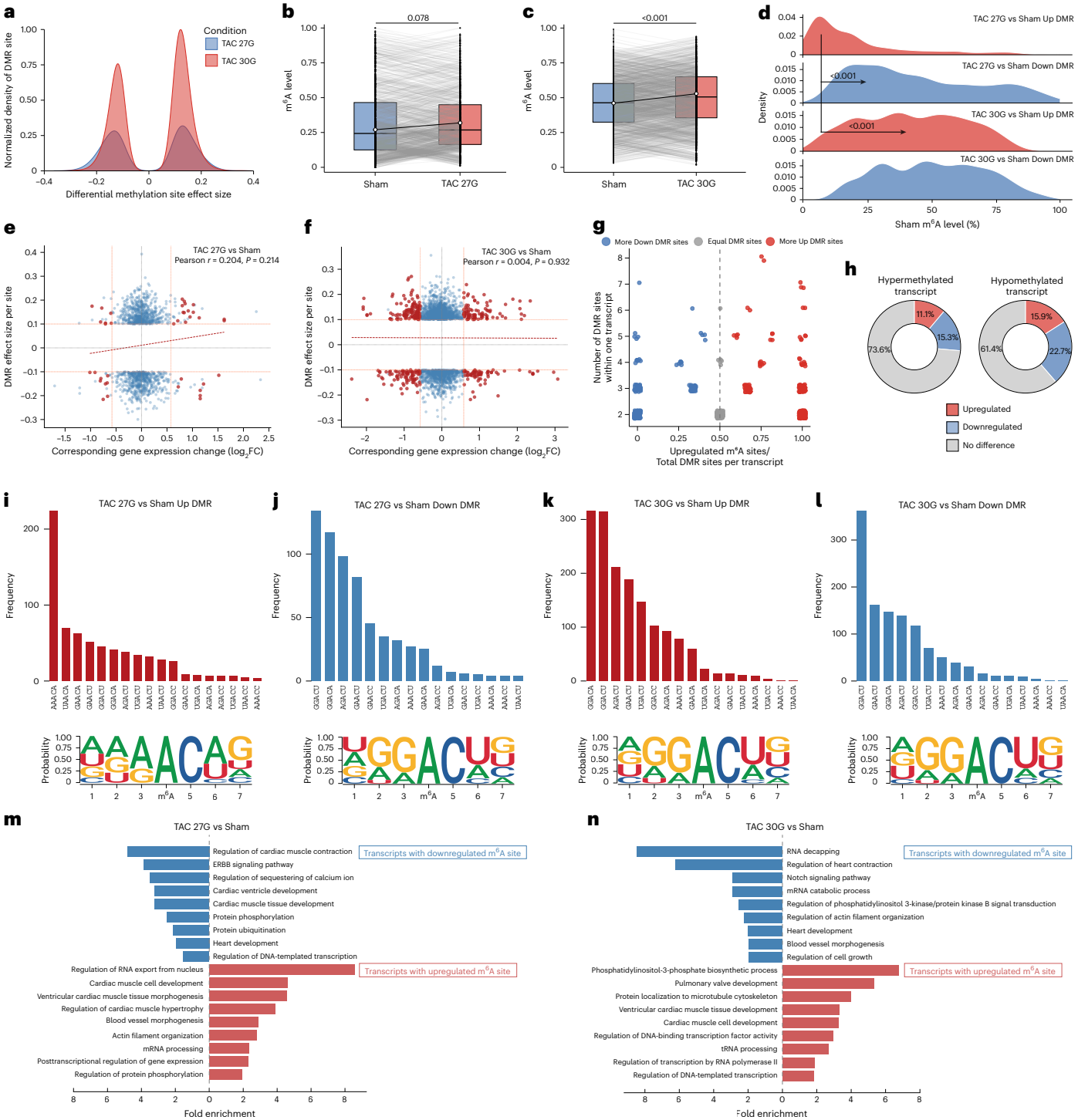


Fig. 4 | DMR sites and enriched pathways. a, Density plot of DMR sites comparing TAC 27G versus sham (blue, $n = 3$ for each group) and TAC 30G versus sham (red, $n = 4$ for each group). **b**,**c**, Box plot of m^{6}A levels of DMR sites of TAC 27G (**b**, $n = 1{,}335$) and TAC 30G (**c**, $n = 2{,}756$) datasets. Boxes span the 25th to 75th percentiles, center lines indicate medians, and whiskers extend to the most extreme observations within 1.5 times the interquartile range. Gray lines indicate per-site changes, and white dots represent mean values. **d**, Distribution of baseline (Sham) m^{6}A levels for DMR sites, including upregulated DMR sites (Up; red) and downregulated DMR sites (Down; blue) from two TAC datasets. **e**,**f**, Scatter plot showing the relationship between DMR changes and corresponding gene expression changes in the TAC 27G (**e**) and TAC 30G (**f**) datasets. Each point represents a DMR site paired with its corresponding gene expression change. Red points represent the gene changes of the pairs that met DEG thresholds, while blue points represent those that did not meet DEG thresholds. The dashed red line shows the linear regression fit of the red points, with the corresponding Pearson's correlation coefficient (r) and P value provided. **g**, Scatter plot of direction scores (upregulated DMR sites/total DMR sites) for transcripts with ≥2 DMR sites. Each dot represents an individual transcript, colored by regulatory trend (red, more upregulated sites; blue, more downregulated sites; gray, equal proportions). **h**, Proportion of hypermethylated transcripts (left) or hypomethylated transcripts (right) that are upregulated (adjusted $P < 0.05$, positive $\log_2$FC), downregulated (adjusted $P < 0.05$, negative $\log_2$FC) or unchanged (adjusted $P > 0.05$) based on gene expression in DGE analysis. **i**–**l**, Motif frequency distribution and enrichment analyses of DMR sites, including upregulated (**i**) and downregulated (**j**) sites in TAC 27G and upregulated (**k**) and downregulated (**l**) sites in TAC 30G datasets. **m**,**n**, GO biological process analysis of transcripts containing upregulated (red) and downregulated (blue) DMR sites in TAC 27G (**m**) and TAC 30G (**n**) datasets. P values are annotated to show statistical significance. Statistics was performed using paired two-sided Wilcoxon signed-rank test in **b** and **c**, two-sided Wilcoxon rank-sum test in **d**, or two-sided Pearson correlation analysis in **e** and **f**.

significant changes in gene expression (Fig. 4h). In addition, we integrated differential poly(A) tail length profiling with our DMR results to evaluate potential cross-talk among poly(A) tail dynamics, m^{6}A remodeling and gene expression during heart failure (Extended Data Fig. 2a–e and Supplementary Table 4). Profiling revealed over 200 differential poly(A) tail length events in 30G mice, compared to none in 27G mice. Nonetheless, poly(A) tail dynamics showed no transcriptome-wide correlation with either DMRs or DEGs.

Motif enrichment analysis of DMR sites provided additional insights into m^{6}A regulatory patterns in heart failure. In 27G mice, the most frequent motif for upregulated m^{6}A sites was AAACA, which occurred at ~3 times the frequency of the second most common motif, and the top three motifs were generalized to the DAACA pattern (Fig. 4i). For downregulated m^{6}A sites in 27G mice, the most frequent motif was GGACU (Fig. 4j). In 30G mice, the top two motifs for upregulated m^{6}A sites were GGACA and GGACU (Fig. 4k). For downregulated sites in 30G mice, GGACU was dominant (Fig. 4l).

For GO biological process enrichment, transcripts with upregulated m^{6}A sites in 27G mice were enriched for RNA-related processes, including RNA export and posttranscriptional gene regulation, as well as cardiac-related processes, including cardiac muscle development, morphogenesis and hypertrophy. Transcripts with downregulated m^{6}A sites in 27G mice were associated with cardiac muscle contraction and ventricular development (Fig. 4m). In 30G mice, transcripts with upregulated m^{6}A sites were enriched in phosphatidylinositol 3-phosphate biosynthesis, cardiac muscle development and transcriptional regulation. Transcripts with downregulated m^{6}A sites were associated with RNA decapping and catabolic processes, as well as heart contraction and development (Fig. 4n). Collectively, these findings suggest that m^{6}A modifications in heart failure predominantly targeted transcripts involved in RNA regulation and metabolism, as well as cardiac development and function.

Conserved m^{6}A patterns between mouse and human heart failure

To assess the conservation of m^{6}A regulation in heart failure between mice and humans, we compared our dataset with published m^{6}A profiles from human failing heart samples by MeRIP-seq[14]. The comparison focused on overlapping m^{6}A regulatory trends at both the transcript and locus levels. DMR sites from the mouse heart failure model were aligned with differentially enriched m^{6}A peaks from the human dataset (Fig. 5a). Transcript-level comparison identified 227 overlapping transcripts between the 1,055 transcripts containing upregulated m^{6}A sites in TAC 30G mouse hearts and the 780 transcripts harboring enriched peaks in human failing hearts. Similarly, 95 overlapping transcripts were found between the 827 transcripts with upregulated sites from sham mouse hearts and the 698 transcripts from enriched peaks in human nonfailing hearts (Fig. 5b). At the locus level, 490 sites with overlapping transcript symbols in human-enriched m^{6}A peaks were selected to align their genomic coordinates with the corresponding converted peak regions. This comparison revealed 198 sites (40.4%) located in the peaks, 27 sites (5.5%) positioned in nearby peak regions and 265 sites (54.1%) in regions unrelated to the peaks (Fig. 5c,d and Supplementary Table 5). From these overlapping results, we selected three representative transcripts containing multiple DMR sites for detailed site–peak mapping.

Nuclear paraspeckle assembly transcript 1 (*Neat1*) is a long noncoding RNA with m^{6}A modifications predominantly at the 5′ and 3′ ends (Fig. 5e). Only the 5′ end region showed high levels of m^{6}A, and all seven upregulated m^{6}A sites in TAC 30G mice located to this region. In human failing hearts, one differentially enriched peak was identified in *NEAT1*. After coordinate conversion, five of the seven DMR sites mapped precisely to this peak, with one additional site located within 20 nt of the peak boundary.

Insulin-like growth factor 1 receptor (*Igf1r*) is a multi-exon transcript with multiple highly modified sites located in the first, second and last exons (Fig. 5f). In TAC 30G mice, four upregulated m^{6}A sites were identified, with three located in the second exon and one in the last exon. In human failing hearts, two differentially enriched peaks were detected. After conversion, all three second-exon DMR sites mapped to the human peak region. Although the last-exon DMR site did not fall directly within the human peak, this region contained a cluster of highly modified sites, suggesting that cumulative m^{6}A changes may contribute to the locally enriched signal observed in human data.

Synaptopodin 2-like (*Synpo2l*) contained three downregulated m^{6}A sites in the last exon and was a hypomethylated transcript by our definition (Fig. 5g). In human nonfailing hearts, three differentially enriched peaks were detected. After conversion, all three peaks mapped or partially overlapped to the last exon of *Synpo2l*. Two of the three mouse DMR sites fell inside the same human peak region, while the remaining site mapped to another peak.

To further support the reliability of cross-species comparison, we performed orthogonal validation using GLORI in human dilated cardiomyopathy (DCM) samples (Fig. 5h). We selected human transcript *NEAT1* and designed primers targeting converted mouse regions enriched for m^{6}A sites identified by DRS. GLORI followed by Sanger sequencing confirmed the presence of the corresponding number of m^{6}A sites within this region, supporting the validity of our cross-species comparison strategy.

Collectively, our analysis between mouse and human hearts shows consistent examples where conserved m^{6}A regulatory features in heart failure may present as either gains or losses of modification and are preserved at both transcript and locus levels.

Joint transcriptomic and epitranscriptomic m^{6}A analyses show isoform-specific m^{6}A dynamics in heart failure

Differential transcript usage (DTU) analysis identified 416 events in TAC 30G versus sham mice (Supplementary Table 6). Transcripts with DTU events and DMR sites overlapped at 43 transcripts (Fig. 6a). Ten transcripts showed further intersection compared to transcripts of differentially enriched peaks in human heart samples, including the representative example *Synpo2l*. We therefore examined *Synpo2l* for isoform usage and m^{6}A regulation. Three *Synpo2l* isoforms are detectable in the mouse heart, with two annotated in the comprehensive gene annotation reference and one isoform without an Ensembl Transcript ID. While all three isoforms share a common last exon, their upstream exons are unique (Fig. 6b). Isoform 1 was the most abundant in sham mice, accounting for 63.56% of total expression, followed by isoform 3 (23.28%) and isoform 2 (13.16%). By contrast, in TAC 30G mice, isoform 3 was the most predominant, accounting for 77.75% of total expression, while isoform 1 decreased to 14.02% and isoform 2 to 8.23% (Fig. 6c). Although all three isoforms were significantly upregulated in TAC 30G mice, their fold changes differed markedly. DRS showed that isoform 1 increased 1.5-fold, isoform 2 increased 3.8-fold and isoform 3 increased 18.4-fold (Fig. 6d). These results were validated by quantitative real-time PCR (qRT-PCR), which confirmed increases of 1.9-fold, 4.4-fold and 15.5-fold for isoforms 1–3, respectively (Fig. 6e). Despite exclusion of TAC 27G data from DTU analysis because of sequencing quality, qRT-PCR showed similar regulation (Extended Data Fig. 3a). Exogenous overexpression of each isoform with a C-terminal FLAG tag in HEK293T cells enabled identification of isoform-specific bands, with isoform 1 migrating just above 140 kDa, isoform 2 just above 100 kDa and isoform 3 at ~75 kDa (Fig. 6f, lanes 9–14). Isoform 2 also produced an ~75-kDa FLAG-positive band (lane 13), potentially reflecting alternative translation initiation at the downstream isoform 3 start codon within the shared terminal exon. Endogenous isoforms 2 and 3 increased significantly in TAC 30G mice by 1.68- and 17.09-fold, respectively, whereas isoform 1 showed no significant change (Fig. 6f,g, lanes 1–8).

We identified 11 sites in the shared last exon with average m^{6}A levels above 10% in all three isoforms. Only site 7 in isoform 3 was downregulated in TAC 30G versus sham mice, corresponding to one of

https://doi.org/10.1038/s44161-026-00898-0

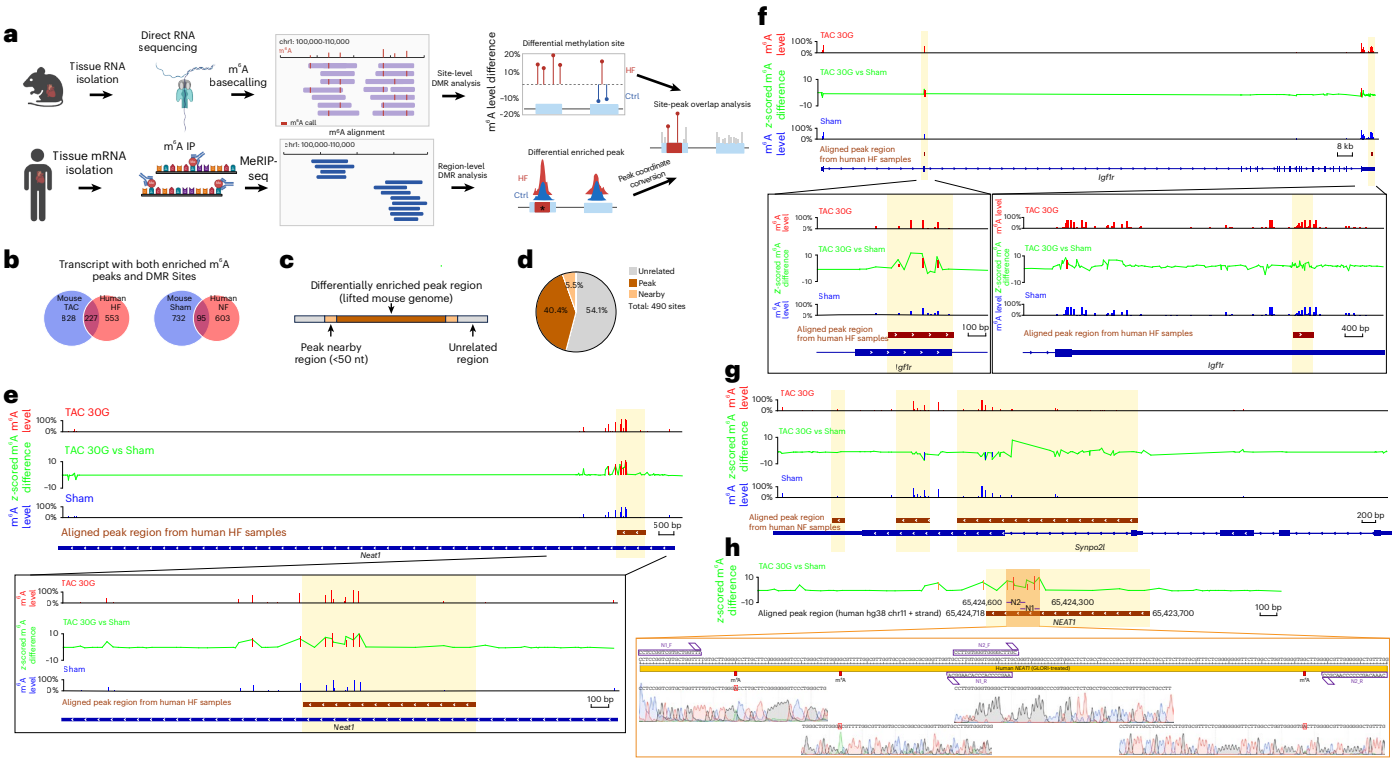


Fig. 5 | Conserved m^{6}A patterns between mouse and human heart failure. **a**, General schematic for human–mouse cross-species m^{6}A site-peak overlap analysis. Mouse heart samples were analyzed by DRS followed by DMR analysis to identify DMR sites, and human heart samples were analyzed by MeRIP-seq followed by exomePeak analysis to identify differentially enriched peaks. Sites and peaks were mapped to determine their overlap. **b**, Venn diagrams of transcripts with both DMR sites in mouse (blue) and differentially enriched m^{6}A peaks in human (red), including the comparison between TAC mouse heart and human failing (HF) heart (left) and between sham mouse heart and human nonfailing (NF) heart (right). **c**, Illustration of the relative positions of DMR sites and the converted peak regions: sites located within the peak (brown), sites located near the peak (<50 nucleotides; nude) and sites located in regions unrelated to the peak (gray). **d**, Proportion of DMR sites falling into the three positional categories relative to the converted peak regions. **e**–**g**, Visualization of m^{6}A site-peak overlap of transcript *Neat1* (**e**), *Igf1r* (**f**) and *Synpo2l* (**g**), generated with Integrative Genomics Viewer. m^{6}A sites with corresponding m^{6}A levels are shown as bar plots for TAC 30G mice (top row, red) and sham mice (third row, light blue) across the reference mouse transcriptome (fifth row, dark blue). The line plot (second row, green) shows the *z*-scored m^{6}A level difference between the two groups, with DMR sites annotated along the curve. The coordinates of differentially enriched peaks in human samples are converted and aligned to mouse transcriptome (fourth, brown). The overlapping regions of the peaks in mouse transcriptome are filled with yellow. **h**, GLORI validation of candidate DMR sites in human transcript *NEAT1*. DMR sites in mouse *Neat1* are annotated (orange bar) on the line plot (top row, green). Human m^{6}A peak is filled with yellow, with primer-targeted region filled with orange. Sites covered by GLORI-based primer pairs (N1 and N2, purple) are highlighted in red bars. Predicted *NEAT1* GLORI-treated sequence is shown in the second row, and the sequencing results with chromatogram are shown in the third row. Panel **a** created in BioRender; Xu, Z. https://biorender.com/v6saygp (2026).

the three *Synpo2l* DMR sites identified globally (Fig. 6h–j). To explain the remaining DMRs, we compared methylation across isoforms. Sites were classified as different m^{6}A level or similar m^{6}A level when the highest and lowest isoform-specific levels differed by >10% or <5%, respectively. Similar-m^{6}A-level sites 8–10 lay toward the exon end, whereas different-m^{6}A-level sites 1, 2, 3, 6 and 7 were concentrated near its beginning (Fig. 6k). At the latter sites, isoform 1 consistently had the highest m^{6}A levels and isoform 3 the lowest. Isoform 1 also contained significantly more m^{6}A sites per transcript in the last exon, whereas isoform 3 contained fewer (Fig. 6l).

Altogether, these findings indicate that the classification of *Synpo2l* as a hypomethylated transcript in heart failure is not explained by the loss of m^{6}A within the same transcript but rather by isoform switching toward a transcript isoform that intrinsically carried fewer modifications. This highlights the phenomenon that transcript isoforms may carry different levels of m^{6}A modifications, and an isoform-unique m^{6}A pattern in different isoforms of the same gene may exist.

Differential promoter activity regulates *SYNPO2L* isoform expression

In the human transcriptome, similar *SYNPO2L* isoforms were identified by coordinate conversion and validated by PCR and Sanger sequencing (Fig. 7a). In this case, two unannotated isoforms, termed isoform 3-a and 3-b, were detected, differing only in the 5′ UTR, with isoform 3-b containing an 80-nt extension of the first exon. FANTOM5 TSS (transcription start site) peaks and cap analysis of gene expression read counts indicated that the two isoforms share the same TSS, whereas isoforms 1 and 2 have distinct TSSs[31]. Given their identical coding sequences and shared TSS, these two isoforms were not distinguished in subsequent analyses and were collectively referred to as isoform 3.

In human DCM hearts, isoform 3 RNA expression was again significantly upregulated compared with nonfailing controls, whereas isoforms 1 and 2 showed no change (Fig. 7b). This was consistent also at the protein level by western blotting (Fig. 7c,d). In human pluripotent stem cell-derived cardiomyocytes (hSC-CM), endothelin-1 (ET-1) can be used to stimulate cardiac stress and contractile dysfunction[32]. In this cellular model, RNA expression of *SYNPO2L* isoforms 2 and 3 were significantly upregulated after ET-1 treatment, together with archetypal cardiac stress markers *NPPA*, *MYH7* and *ACTA1* (Fig. 7e,f). The results suggest a link between cardiac stress induction and *SYNPO2L* isoform changes.

To assess how *SYNPO2L* isoforms use distinct TSSs, we cloned their respective promoters and performed luciferase reporter assays in hSC-CM (Fig. 7g). Isoform 1 and 2 promoters corresponded to ENCODE4

https://doi.org/10.1038/s44161-026-00898-0

candidate *cis*-regulatory elements EH38E2908507 and EH38E1478396, respectively[33]; the isoform 3 promoter was empirically defined as 350 nt upstream of its TSS and subsequently extended to 1,000 and 1,500 nt. At baseline, isoform 1 and 2 promoters exceeded 400-fold activity relative to the minimal promoter. The 350-nt and 1,000-nt isoform 3 constructs showed minimal activity (~1.8- and 2.0-fold), whereas the 1,500-nt construct showed ~23.9-fold activity (Fig. 7h). The 1,500-nt region overlaps with the promoter of isoform 2, such that transcription of isoform 3 may rely on a shared promoter with isoform 2. ET-1 reduced isoform 1 promoter activity, left isoform 2 and the shorter isoform 3 constructs unchanged and increased activity of the 1,500-nt construct (Fig. 7i). A putative upstream distal regulatory element (DRE) was identified from a *SYNPO2L* splicing quantitative trait locus (rs10824026) associated with increased isoform 3 usage[34], within a region of high histone modification activity (Extended Data Fig. 3b). At baseline, the DRE reduced isoform 1 promoter activity and increased isoform 2 and 3

Fig. 6 | Joint transcriptomic and epitranscriptomic m^{6}A analyses show isoform-specific m^{6}A dynamics in heart failure. a, Venn diagram of transcripts with both DMR sites (blue) and DTU events (red). **b**, Transcript structure of *Synpo2l* isoforms annotated on mouse transcriptome, including isoform 1 (brown), isoform 2 (blue) and isoform 3 (pink). **c**, Proportion of each *Synpo2l* transcript isoform in sham and TAC 30G ($n = 4$ for each group). **d**, Transcript counts per million reads (CPM) of each isoform by DRS in sham versus TAC 30G ($n = 4$ for each group). **e**, Relative fold change of each isoform by qRT-PCR in sham versus TAC 30G ($n = 4$ for each group). **f**, Western blotting for SYNPO2L in sham versus TAC 30G mouse hearts (sham, lanes 1–4; TAC 30G, lanes 5–8), and in HEK293T cells overexpressing FLAG-tagged SYNPO2L isoforms (isoform 1, lanes 9 and 12; isoform 2, lanes 10 and 13; isoform 3, lanes 11 and 14), probed for SYNPO2L (lanes 1–11) and FLAG (lanes 12–14), with total protein staining as a loading control. **g**, Quantification of western blots on endogenous SYNPO2L isoform abundance in sham versus TAC 30G ($n = 4$ for each group). **h**–**j**, m^{6}A levels of 11 sites at the common last exon for isoform 1 (**h**), isoform 2 (**i**) and isoform 3 (**j**) in sham and TAC 30G. Site meeting DMR criteria at isoform level is marked with an asterisk. **k**, Average m^{6}A levels of 11 m^{6}A sites at the common last exon for three isoforms; sites identified as DMR at transcript level are marked with asterisks. **l**, Violin plot of the number of m^{6}A sites per transcript in the last exon for the three isoforms. Inset boxes show the median and 25th to 75th percentiles; whiskers extend to the most extreme observations within 1.5 times the interquartile range. Data are shown as mean ± s.e.m. *P* values are annotated to show statistical significance. Statistics was performed using unpaired two-tailed Student's *t*-test in **d**, **e** and **g**, or Kruskal–Wallis test with Dunn's post hoc test and Benjamini–Hochberg correction in **l**.

activity (Fig. 7j). With the DRE present, ET-1 similarly decreased isoform 1 and increased isoform 3 promoter activity (Fig. 7k).

Altogether, these results indicate that a coordinated regulatory mechanism involving promoter usage, DRE responsiveness and TSS selection contributes to isoform-specific regulation of *SYNPO2L*.

Direct and indirect effects of m^{6}A modification on *SYNPO2L* isoform regulation

To examine the relationship between m^{6}A regulation and *SYNPO2L* isoform expression, m^{6}A writers (*METTL3*, *METTL14* and *METTL16*), along with catalytic mutants (*METTL3 D395A* and *METTL14 R298P*[35]) and negative control blue fluorescent protein (BFP), were overexpressed in hSC-CMs. Isoform 3 was significantly upregulated in *METTL3* and *METTL14* wild-type (WT) conditions (~1.5- and 1.3-fold, respectively) compared with mutant and control groups, while isoform 2 showed a modest increase (~1.2-fold, $P = 0.076$) in *METTL3* WT condition compared with BFP control group (Fig. 8a). The same set of cardiac stress markers *NPPA*, *MYH7* and *ACTA1* were also upregulated in *METTL3* WT, while only *NPPA* was upregulated significantly in *METTL14* WT (Fig. 8b). These results suggest that the overexpression of m^{6}A writer, especially *METTL3*, induces a stress-like response. To validate this hypothesis, we performed a luciferase reporter assay using the 1,500-nt sequence encompassing the isoform 2/3 promoter which contains the stress-responsive element. Co-transfection with *METTL3* WT showed a trend toward elevated promoter activity ($P = 0.068$), consistent with possible *METTL3* activation of the stress-responsive promoter governing *SYNPO2L* isoform expression (Fig. 8c). These findings support indirect coupling of m^{6}A regulation and *SYNPO2L* isoform switching through cardiac stress induction.

To investigate how METTL3 activity regulates *SYNPO2L* expression beyond cardiac stress signaling, we subjected hSC-CMs to a 2 × 2 factorial treatment combining ET-1 stimulation and METTL3 catalytic inhibition via STM2457. ET-1 and STM2457 individually upregulated *SYNPO2L* Isoform 2 (~3.3- and 1.4-fold, respectively) and isoform 3 (~5.0- and 1.3-fold, respectively), with ET-1 exerting a markedly stronger inductive effect (Fig. 8d). Combined treatment increased isoforms 1, 2 and 3 to ~1.6-fold, ~5.7-fold and ~6.4-fold of untreated control levels, respectively, with all three significantly higher than under ET-1 alone. Conversely, STM2457 reduced basal *MYH7* and *ACTA1* expression and significantly attenuated their ET-1-induced upregulation (Fig. 8e). Combined treatment also reduced *NPPA* expression by approximately 22% relative to ET-1 alone, although this difference was not significant ($P = 0.097$).

To determine whether m^{6}A levels on *SYNPO2L* were directly altered, we performed MeRIP-qPCR at both the total gene and isoform-specific levels. Total *SYNPO2L* m^{6}A enrichment decreased upon ET-1 (~3.6-fold) and STM2457 treatment (~7.0-fold), with combined treatment yielding a further reduction (~20.4-fold; Fig. 8f). Having previously linked reduced gene-level m^{6}A enrichment in the mouse heart failure model to the preferential accumulation of isoform 3, which carries fewer m^{6}A modifications, we investigated whether a similar mechanism operates in a human-derived cellular model. Isoform-specific MeRIP-qPCR revealed that m^{6}A enrichment on isoforms 1 and 2 decreased exclusively upon STM2457 treatment but remained unaffected by ET-1 alone (Fig. 8g,h). For isoform 3, ET-1 alone was associated with an approximately 1.7-fold reduction in m^{6}A enrichment, but this difference was not statistically significant ($P = 0.619$). STM2457 alone and in combination with ET-1 significantly reduced isoform 3 m^{6}A enrichment relative to untreated controls (Fig. 8i). These findings prompted us to hypothesize that METTL3 inhibition and ET-1 signaling operate through distinct mechanisms and raised the possibility that METTL3 inhibition may directly regulate *SYNPO2L* transcript turnover. Actinomycin D mRNA stability assays in hSC-CMs revealed that STM2457 treatment significantly prolonged the half-lives of isoform 2 and isoform 3 but not isoform 1 (Fig. 8j–l). Estimated decay constants (k) indicated that isoform 1 showed the highest stability under both control and STM2457-treated conditions, followed by isoform 2 and isoform 3.

To summarize, our results dissect the multi-layered posttranscriptional regulation governing *SYNPO2L* isoform expression by m^{6}A machinery. While m^{6}A writer overexpression indirectly triggers specific *SYNPO2L* isoform transcription by initiating cardiac stress signaling, m^{6}A deposition directly targets *SYNPO2L* isoforms for transcript clearance.

Discussion

In our study, we used ONT DRS to map the transcriptome-wide m^{6}A landscape at base and transcript-isoform resolution in a pressure-overload model of heart failure. We find that extensive and dynamic m^{6}A remodeling occurs in heart failure. Moreover, our results reveal the presence of transcript isoform-specific m^{6}A differences, potentially confounding assessment methods that do not take unique isoform details into account.

The DRACH-context m^{6}A model implemented in Dorado prioritized high-confidence site detection, trading coverage for accuracy. This strategy and continued improvements in ONT basecalling provide a framework for refining m^{6}A annotation and extending detection to other RNA modifications[36]. DRS enabled us to map cardiac m^{6}A distribution, identify highly modified sites and rank motifs by modification probability. Consistent with previous reports, GGACU was the most frequently methylated motif[10,17]. Highly modified sites also clustered and favored accessible RNA structures[29].

Differential m^{6}A regulation represents the central focus of this study. We evaluated the relationship between m^{6}A status and gene expression at both site and transcript levels. DMR–DEG comparisons revealed no global correlation, including when analysis was restricted to transcripts with multiple consistently regulated sites. A previous cardiomyocyte DRS study similarly found no correlation between transcript m^{6}A rank and relative abundance, whereas mouse heart MeRIP-seq analysis reported a positive correlation between methylation and expression[15,37]. Platform or analytical differences may explain this discrepancy. Likewise, transcriptome-wide analysis revealed no global correlation between m^{6}A remodeling and poly(A) tail length dynamics. Nonetheless, the absence of a global correlation does

https://doi.org/10.1038/s44161-026-00898-0

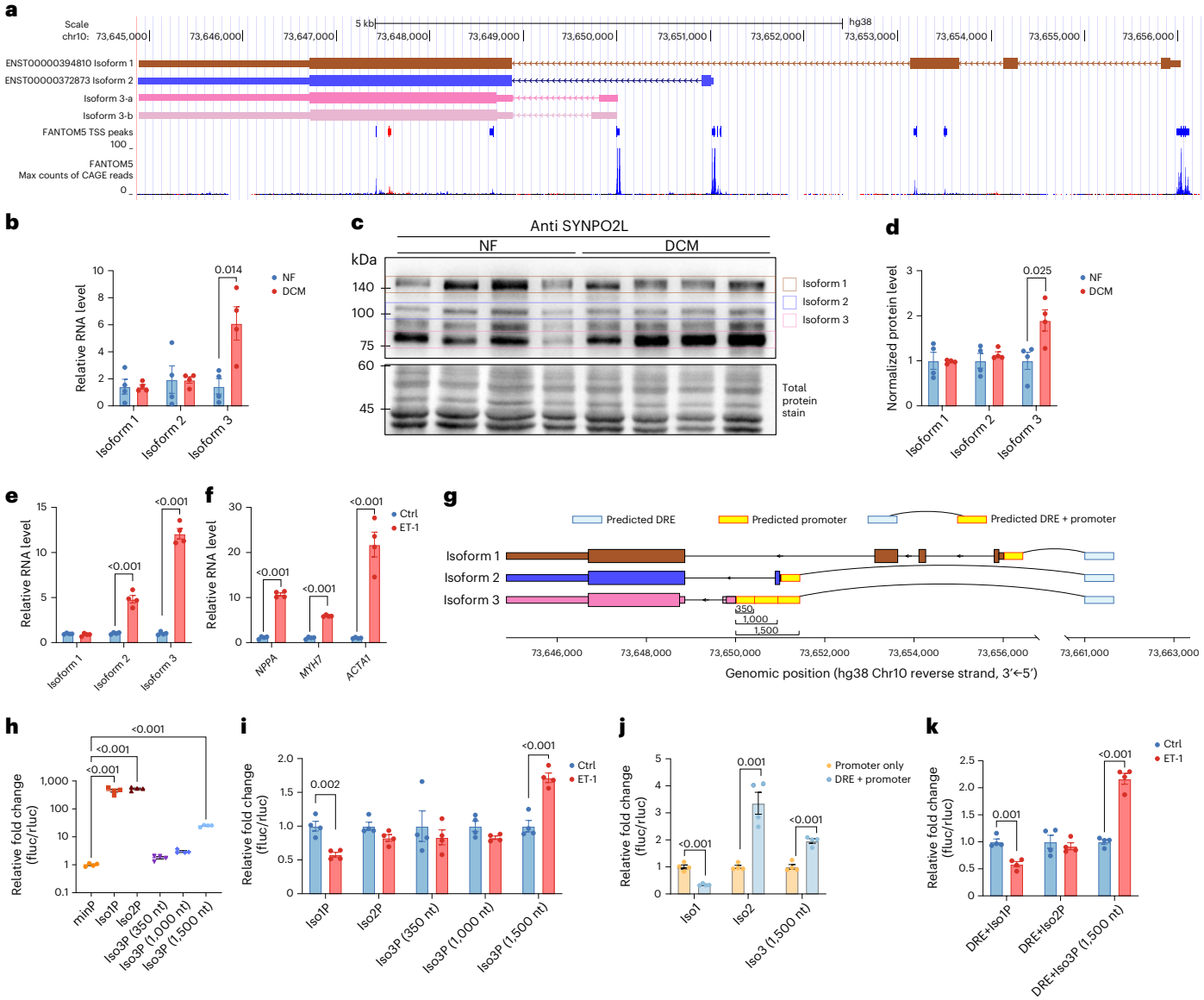


Fig. 7 | Differential promoter activity regulates *SYNPO2L* isoform expression. **a**, Transcript structure of human *SYNPO2L* isoforms, including isoform 1 (brown), isoform 2 (blue), isoform 3-a (pink) and isoform 3-b (light purple). Accompanying FANTOM5 TSS peaks and max counts of cap analysis of gene expression (CAGE) reads panels are retrieved from UCSC Genome Browser[57]. **b**, Relative fold change of each isoform by qRT-PCR in NF versus DCM samples ($n = 4$ for each group). **c**, Western blotting for SYNPO2L isoforms in NF and DCM samples. **d**, Quantification of SYNPO2L isoform abundance from western blots ($n = 4$ for each group). **e**, Relative fold change of each *SYNPO2L* isoform by qRT-PCR in control versus ET-1-treated hSC-CMs ($n = 4$ for each group). **f**, Relative fold change of cardiac stress markers by qRT-PCR in control versus ET-1-treated hSC-CMs. **g**, Schematic of luciferase reporter constructs showing isoform-specific promoters of *SYNPO2L* (genomic coordinates: Iso1P, 73655944–73656293; Iso2P, 73651044–73651354; Iso3P (350 nt), 73649920–73650270; Iso3P (1,000 nt), 73649920–73650920; Iso3P (1,500 nt), 73649920–73651354) and a putative DRE (73661006–73661719). **h**, Normalized luminescence intensity driven by isoform-specific promoters at baseline control culture condition ($n = 4$ for each group). **i**, Relative normalized luminescence intensity driven by isoform-specific promoters in control versus ET-1-treated hSC-CMs ($n = 4$ for each group). **j**, Relative normalized luminescence intensity driven by isoform-specific promoters only versus DRE plus isoform-specific promoters at baseline control culture condition ($n = 4$ for each group). **k**, Relative normalized luminescence intensity driven by DRE-promoter combinations under control and ET-1 conditions ($n = 4$ for each group). Data are shown as mean ± s.e.m. *P* values are annotated to show statistical significance. Statistics was performed using unpaired two-tailed Student's *t*-test in **b**–**f** and **i**–**k**, or one-way ANOVA followed by planned pairwise comparisons with Benjamini–Hochberg correction performed on $\log_{10}$-transformed data in **h**.

not exclude target-specific cross-talk, as m^{6}A deposition is known to recruit deadenylation complexes to shorten poly(A) tails on specific transcripts[38]. Indeed, the functional impact of m^{6}A may depend on site-specific recognition by reader proteins such as IGF2BP and YTHDF family members, underscoring the importance of studying m^{6}A function at site level[39,40]. Motif enrichment also differed between TAC models, where AAACA is enriched in upregulated sites in 27G mice and GGACR is dominant in 30G mice, consistent with the differences observed in their basal m^{6}A levels and suggesting distinct regulatory mechanisms at different stages of heart failure. This may be also related to the differential expression of m^{6}A regulatory proteins observed across disease stages.

Cross-species comparison revealed conserved m^{6}A regulation between mouse and human heart failure. Representative transcripts with site-to-peak overlaps, including *Neat1*, *Igf1r* and *Synpo2l*, are known m^{6}A substrates whose methylation can alter reader interactions

https://doi.org/10.1038/s44161-026-00898-0

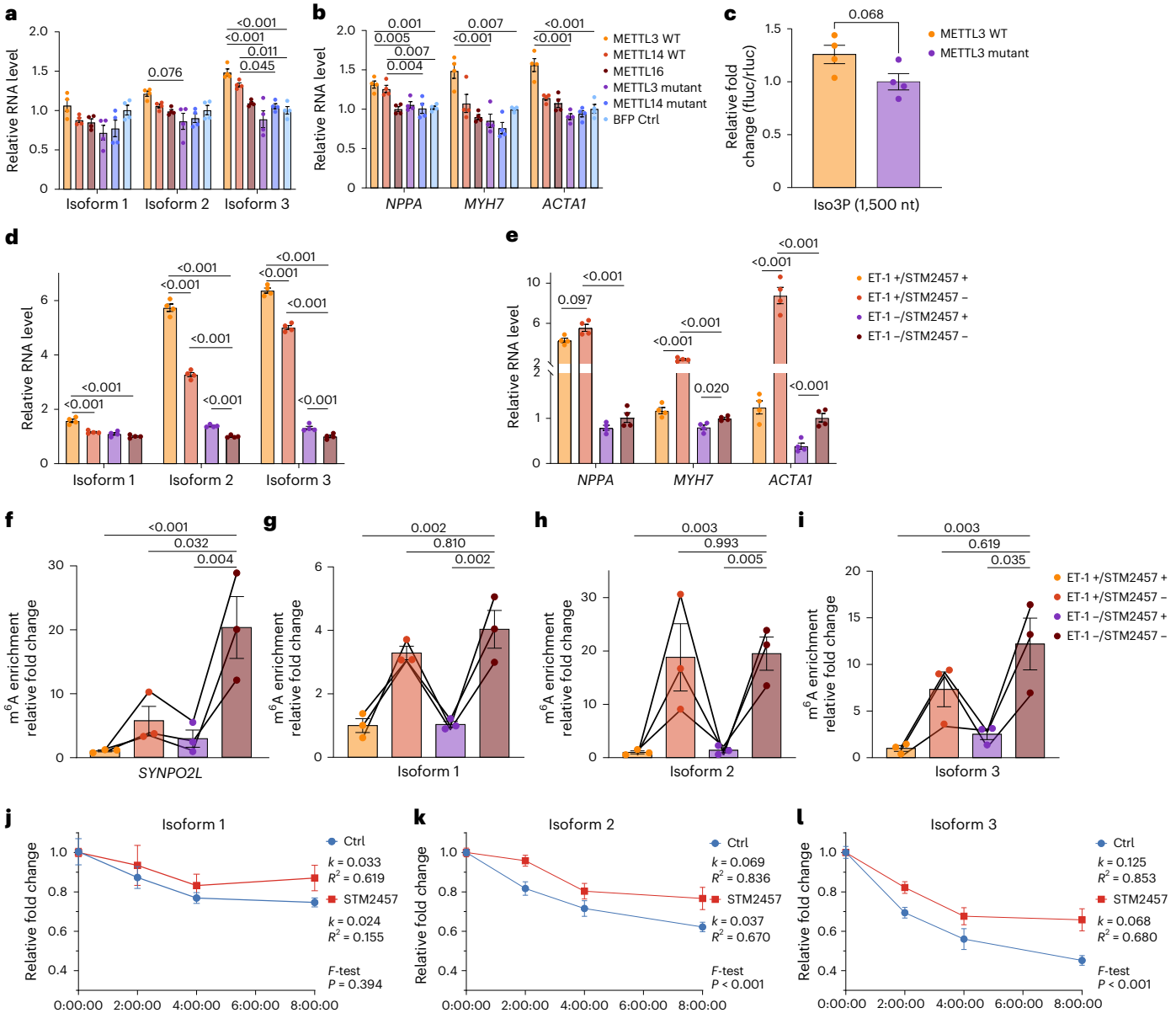


Fig. 8 | Direct and indirect effects of m^{6}A modification on *SYNPO2L* isoform regulation. a, Relative fold change of each *SYNPO2L* isoform by qRT-PCR following overexpression of m^{6}A writers (WT and mutant) and negative control BFP in hSC-CMs ($n = 4$ for each group). **b**, Relative fold change of cardiac stress markers by qRT-PCR under m^{6}A writer overexpression conditions. **c**, Relative normalized luminescence intensity driven by Iso3P (1,500 nt) in METTL3 WT versus METTL3 mutant in hSC-CMs ($n = 4$ for each group). **d**, Relative fold change of each *SYNPO2L* isoform by qRT-PCR following a 2 × 2 factorial treatment combining ET-1 stimulation and METTL3 catalytic inhibition via STM2457 in hSC-CMs ($n = 4$ for each group). **e**, Relative fold change of cardiac stress markers by qRT-PCR under the 2 × 2 factorial treatment. **f**–**i**, Relative fold change of m^{6}A enrichment of *SYNPO2L* transcript (**f**), isoform 1 (**g**), isoform 2 (**h**) and isoform 3 (**i**) by MeRIP-qPCR following the 2 × 2 factorial treatment ($n = 3$ for each group). **j**–**l**, Relative fold change of *SYNPO2L* isoform 1 (**j**), isoform 2 (**k**) and isoform 3 (**l**) by qRT-PCR following STM2457 or control treatment and then under 8 h actinomycin D chasing in hSC-CMs ($n = 3$ for each group). Data are shown as mean ± s.e.m. *P* values are annotated to show statistical significance. Statistics was performed using one-way ANOVA followed by planned pairwise comparisons with Sidak's post hoc test performed on $\log_2$-transformed data in **a**, **b**, **d** and **e**, unpaired two-tailed Student's *t*-test in **c**, one-way repeated measures ANOVA with Sidak's post hoc test performed on $\log_2$-transformed data in **f**–**i**, or the extra sum-of-squares *F*-test following one-phase exponential decay fitting in **j**–**l**.

and influence genome stability or transcriptional regulation[41–44]. GLORI validated predicted sites within enriched human peaks, highlighting the feasibility of coordinate conversion for enhancing the resolution of MeRIP-seq and enabling site-specific investigation when human relevance is established.

Isoform-resolved DRS analysis indicated that reduced average *Synpo2l* methylation largely reflected switching toward a transcript variant carrying fewer modifications, highlighting the importance of both base- and isoform-level analysis. *SYNPO2L* contributes to cardiac structural organization and contractile function, with splice variants linked to atrial fibrillation[45,46]. We observed similar isoform switching in human heart failure. While two previous genome-wide association studies reported the third unannotated isoform as noncoding or identified associated splicing quantitative trait loci, our wet-lab experimental data support their splicing condition and protein-coding potential[34,47]. Cardiomyocyte reporter assays linked stress-inducible isoform switching to differential promoter activity, supporting a shared isoform 2/3 promoter region and additional regulatory sequence contributions. m^{6}A writer overexpression, particularly METTL3, also induced a stress-like response and isoform switching, suggesting that m^{6}A regulation may

influence this process indirectly[13]. Distinguishing this transcriptional crosstalk from direct m^{6}A effects on *SYNPO2L* mRNA decay explains why both METTL3 overexpression and inhibition alter *SYNPO2L* isoform expression. However, global m^{6}A manipulations produce nonphysiological systemic effects, establishing the precise endogenous role of m^{6}A on *SYNPO2L* in heart failure requires site-specific functional validation.

We acknowledge several potential limitations of this study. Although we quantified common m^{6}A-related enzymes in both TAC models, we did not link individual enzymes to specific sites or explain the differing DMR motif enrichments. Future targeted gain- and loss-of-function approaches will be required to resolve the contributions of individual enzymes to site-specific m^{6}A regulation. Human and mouse datasets were generated using different platforms. Direct comparison between MeRIP-seq and DRS may be affected by differences in sensitivity, resolution and analytical biases. Although GLORI validated selected sites, comprehensive cross-platform concordance was beyond the scope of this study. Future studies performing multiple m^{6}A profiling approaches on the same biological samples will be important to further validate conserved regulatory events. Finally, cross-species validation and isoform analyses primarily used TAC 30G data because suboptimal 27G sequencing generated truncated reads that limited site coverage and isoform annotation.

In conclusion, our study provides a transcriptome-wide, base-resolution m^{6}A landscape in heart failure, identifies conserved regulatory features and reveals isoform-specific m^{6}A dynamics. These findings expand our understanding of m^{6}A regulation and provide a foundation for future studies aimed at identifying therapeutic epitranscriptomic targets in heart failure.

Methods

Ethical statement

This research complies with all relevant ethical regulations. Study protocols for the collection and use of biopsy specimens of human heart samples for research were approved (approval number L12-405) by the National University of Singapore institutional review board committee, in accordance with its guidelines and supervision. All experiments performed with human embryonic stem cells (hESCs) were conducted in accordance with the guidelines and under the supervision of the National University of Singapore institutional review board committee (approval number NUS-IRB-2024-810). Generation and use of the induced pluripotent stem cell (iPSC) line 353 were approved by the ethics commission at RWTH Aachen University Hospital (approval number EK206/09).

Human heart samples

Biopsy specimens of DCM samples were obtained from the apical part of the left ventricular wall from patients with DCM, and biopsy specimens of nonfailing samples were from healthy donors without history of heart failure. Biopsies were snap frozen in liquid nitrogen and transferred for storage at −80 °C until further experiments.

Animals

Adult male C57BL/6J mice (8 weeks old) were used in this study. All animal experimental procedures were approved by the National University of Singapore institutional animal care and use committee and undertaken in strict accordance with the Singapore National Advisory Committee for Laboratory Animal Research guidelines. The original breeding stock was purchased from the Jackson Laboratory, and mice used in this study were bred in-house at the National University of Singapore. Mice were kept in a temperature- and humidity-controlled room, with free access to food and water.

TAC surgery and tissue collection

Mice were randomly assigned to TAC surgery or sham-operated control groups for 4 weeks. For TAC surgery, two types of needles with different gauge sizes were used, 27G (305109, BD) and 30G (305107, BD).

Mice were anesthetized with injected ketamine cocktail (ketamine 7.5 mg ml^{-1} + medetomidine 0.1 mg ml^{-1}; dosage was 0.1 ml per 10 g) into the intraperitoneal cavity. Partial thoracotomy to the second rib was performed and the sternum retracted using a chest retractor. A small piece of a 7.0 silk suture was placed between the innominate and left carotid arteries. Two loose knots were tied around the transverse aorta, and a small piece of a needle was placed parallel to the transverse aorta. In sham control mice, the entire procedure was identical except for the ligation of the aorta. For postoperative analgesia, the mice were injected with buprenorphine (0.1 mg kg^{-1}) intraperitoneally.

Mice in both groups were killed under 4% isoflurane anesthesia. The left ventricle was isolated, sectioned and mixed, divided into aliquots and snap frozen in liquid nitrogen. All tissue samples were then transferred for storage at −80 °C until further experiments.

Echocardiography

Echocardiography was performed 1 day before surgical intervention for baseline measurement and then on a biweekly basis after the surgery. Mice were anesthetized with 4% isofluorane in 100% oxygen, then maintained onto the isolated nose chamber with 1.5% isoflurane. ECG gel was applied onto the mice and scanning initiated with parasternal long and short axis views in B-mode and M-mode. All images were analyzed using Vevo LAB (v1.7.1).

RNA preparation

The left ventricle was lysed by TissueLyser III (QIAGEN) at 25 Hz until there were no visible tissues with 5 mm stainless steel bead (QIAGEN) and TRIzol (Thermo Fisher Scientific). Total RNA was then extracted by TRIzol according to the manufacturer's instructions. The concentration and quality of total RNA was measured by Qubit (Thermo Fisher Scientific) and Bioanalyzer (Agilent). mRNA was extracted from total RNA by VAHTS mRNA Capture Beads 2.0 (Vazyme). mRNA quality was checked by Bioanalyzer 2100 RNA 6000 Pico Kit (Agilent) for the removal of rRNA and tRNA contamination.

LC–MS/MS analysis of RNA modifications

Liquid chromatography-coupled triple quadrupole mass spectrometry (LC–MS/MS) sample preparation followed the previous publication[48]. From each sample, 10 ng mRNA was enzymatically hydrolyzed in a 50-µl digestion cocktail at 37 °C for 6 h and cleaned up using a 10-kDa cutoff filter. Analysis of the mRNA modifications and the four canonical ribonucleosides was conducted by LC–MS/MS and liquid chromatography-coupled diode array detector (LC–DAD), respectively. Modifications include Am, Cm, Gm, m^{6}A, m^{1}A, m^{6}Am, D (dihydrouridine), Y (pseudouridine), m^{3}C/m^{4}C, m^{5}C, ac^{4}C, m^{1}G and m^{7}G. Compounds were analyzed in multiple reaction monitoring mode, and instrument parameters were optimized using a synthetic standard of the modifications. The LC–MS/MS signal intensities of certain modifications were normalized against the LC-DAD signal intensity of the canonical ribonucleosides to correct for variation in RNA quantities. The intensity values for each modification type from samples of the same batch (TAC 27G versus sham or TAC 30G versus sham) were normalized to the average intensity value in the sham group for figure plotting.

Nanopore DRS

Sequencing library was prepared according to the ONT's SQK-RNA004 protocol with a start material of 5 µg total RNA. The RNA–cDNA hybrid library was loaded onto PromethION Flow Cell RNA (FLO-PRO004RA) in PromethION 24 machine. The sequencing run was started on MinKNOW (v25.03.7) with all default settings. Summaries of the DRS run reports for each flow cell are listed in Supplementary Table 7.

Raw sequencing data processing

For post-run modification basecalling, pod5 format raw data for each sample was processed by Dorado (v1.0.0) with rna004_130bps_sup@

v5.1.0 model (m^{6}A_DRACH) to generate bam file with m^{6}A modification annotation (mod_bam). Then, the mod_bam file was aligned by minimap2 (v2.29) to produce aligned mod_bam file. The alignment used GRCm39 primary genome assembly release M37 as the reference genome. Aligned mod_bam files for all samples were processed simultaneously by Bambu (v3.2.4) with comprehensive gene annotation (GRCm39.112.gtf) for transcript quantification and novel transcript isoform discovery. Gene counts, unique transcript counts, extended annotation file and the metadata from the Bambu outputs were used for further analysis[49].

Differential gene expression analysis

Differential gene expression (DGE) analysis was performed using DESeq2 (v1.46.0)[50] with gene-level counts generated by Bambu. Missing count values were replaced with 0; rows sharing the same gene identifier were aggregated by summing counts. Lowly expressed genes were filtered before model fitting. Genes were retained only when the average read count per sample was at least 10 and when nonzero expression was detected in at least n samples (n = the number of samples per group). DESeq2 datasets were constructed using experimental condition as the design factor, with the control group specified as the reference level. Size factors were estimated using the default median-of-ratios method. Differential expression was assessed using the Wald test, and P values were adjusted using the Benjamini–Hochberg method, with DESeq2's default independent filtering enabled. DEGs were selected by applying a cutoff of $\log_2$FC > |0.58| and adjusted $P < 0.05$.

Extraction of m^{6}A call and feature

The base modification probabilities for m^{6}A calls were extracted from the mod_bam files by Modkit (v0.4.2) sample-probes function. The probability threshold for m^{6}A calls was set at 0.8. The m^{6}A calls from the mod_bam file above the threshold were piled up to construct a bedMethyl table for each sample using Modkit pileup function. The probabilities of the m^{6}A calls within specific motifs to be highly modified for each sample were measured by Modkit motif evaluate function.

For transcript-specific m^{6}A call extraction, a sub mod_bam file was created by selecting read IDs that were assigned to the specific transcript by Bambu. The sub mod_bam files were piled up with the same setting above. The number of m^{6}A sites at read level were extracted using Modkit extract calls function.

General m^{6}A analysis and DMR analysis

Grouped bedMethyl files were compressed with bgzip, indexed with tabix and then processed by Modkit dmr pair function to perform DMR analysis. DRACH m^{6}A sites with an average sequencing coverage of more than 20 reads per sample were selected for analysis. In DMR output, the genome coordinate information, m^{6}A levels in different conditions, effect size and maximum a posteriori-based P value were used for further analysis. DMR sites were selected by applying a cutoff of effect size >|0.1| and maximum a posteriori-based $P < 0.05$.

The motifs and gene names mapped to DMR sites were extracted by GenomicRanges (v1.58.0) and rtracklayer (v1.66.0) using GRCm39.112.gtf with the genome coordinate information for each site.

Differential poly(A) tail length analysis

Poly(A) tail lengths and gene assignments were extracted from aligned BAM files of DRS sequencing data. Reads were annotated with gene features using featureCounts (v2.1.1) in long-read mode (-L) with strandedness enabled (-s 1) against the mouse genome annotation. Poly(A) tail lengths were parsed from primary alignments by extracting the pt:i: tag using samtools (v1.9). Reads uniquely assigned to a gene were merged with their corresponding poly(A) tail length measurements and summarized as the per-sample median poly(A) length for each gene; genes with a minimum of 20 supporting reads in every sample were retained for downstream statistical analysis. For each testable gene, a moderated t-test (limma, empirical Bayes shrinkage of variance) was performed on the per-sample median poly(A) lengths to evaluate differential poly(A) tail length between groups. Raw P values were adjusted for multiple testing using the Benjamini–Hochberg procedure. Genes with significantly altered poly(A) tail length were selected using a cutoff of adjusted $P < 0.05$ and |Δ median poly(A) tail length| > 10 (nt).

GO enrichment

The GO analysis was performed using GO Enrichment Analysis (www.geneontology.org, release 2025-07-22)[51,52]. GO biological process categories were selected by applying a cutoff of adjusted $P < 0.05$.

MeRIP-seq data acquisition and genome assembly conversion

The results of exomePeak analysis for human failing and nonfailing heart mRNA m^{6}A MeRIP-seq were obtained from the author of the previous publication[14]. Cutoff false discovery rate was set to 0.05, and fold enrichment was set to 1.5 for filtering differentially enriched peaks between sample groups.

For cross-species genome assembly conversion, the chromosome, start and end coordinates of enriched m^{6}A peak regions in the human genome (GRCh38) were extracted into a bed file and converted to the mouse genome (GRCm39) using UCSC LiftOver tool with all default settings.

DTU analysis

DTU analysis was performed using DRIMSeq (v1.34.0), DEXSeq (1.52.0) and stageR (v1.28.0) following the cited workflow[53]. The input data were the unique transcript counts file generated by Bambu. Using DRIMSeq, transcript was required to have a count of at least 10 in a minimum of n samples and to represent at least 5% of the total expression of its parent gene in a minimum of n samples (n = the number of samples per group). At the gene level, a minimum count of 10 was required across all samples. Following filtering, transcript counts were analyzed using DEXSeq. A DEXSeq dataset was constructed using the design formula comprising sample and exon terms and a condition-by-exon interaction term. Size factors and dispersions were estimated using the DEXSeq framework. DTU was tested by comparing the full model with a reduced model comprising sample and exon terms. DEXSeq results were further analyzed by stageR. Gene-level adjusted P values were obtained using perGeneQValue and supplied to stageR for screening. Unadjusted transcript-level P values were supplied for confirmation. Stage-wise adjustment was performed using DTU method with a target overall false discovery rate of 0.05. Adjusted results were extracted for transcripts belonging to genes that passed the screening stage.

GLORI-based PCR and Sanger sequencing

The experimental procedure followed a published ultrafast, one-pot procedure GLORI 2.0 protocol[54]. For each reaction, 1 µg of total RNA was treated with 50 µl reaction buffer and incubated for 10 min at 50 °C. RNA was purified by ethanol precipitation, and the pellets were dissolved in 50 µl deprotection buffer. The mixture was incubated at 95 °C for 10 min to get GLORI-treated RNA. GLORI-based primer pairs (Supplementary Table 8) were designed to target specific regions of deaminated and reverse-transcribed RNA. PCR products of the expected size were gel-extracted, purified and subjected to Sanger sequencing (1st Base).

hESC/iPSC cell culture and cardiomyocyte differentiation

For experiments using hSC-CMs, both H1-hESCs and iPS cell-353 line were used as biological replicates (n = 2 per cell line). H1-hESCs were obtained from WiCell (WA01, WiCell), and the iPS cell-353 line was obtained from the Kramann's laboratory at RWTH Aachen University Hospital. Stem cell culture and cardiomyocyte differentiation followed

the previous publication[55]. Cells were maintained under standard mammalian cell culture conditions at 37 °C in a humidified incubator containing 5% CO_2. In this study, 650,000 cells per well in a 12-well plate were maintained in mTesR1 medium (STEMCELL Technologies) and were subjected to 7 µM CHIR99021 (STEMCELL Technologies) in RPMI/B27 without insulin (Gibco) on differentiation day 1. On day 3, cells were subjected to 5 µM IWP2 (Sigma Aldrich), and the media was refreshed with RPMI/B27 without insulin after 48 h on day 5. After cardiovascular progenitors were formed on day 7, Cells were maintained in RPMI/B27 with insulin from day 7 onward and refreshed every 3 days. Mature cardiomyocytes were seeded at a density of 80,000 cm^{-2} for downstream experiments from day 14 onward.

ET-1 treatment

Cells were maintained in starvation medium consisting of Williams' E Medium (Gibco) with 1:25 Cell Maintenance Cocktail - B (Gibco, A13448) for 24 h before ET-1 treatment. Cells were then treated with 100 nM ET-1 (TargetMol, T19309) in fresh starvation medium, while an equal volume of DMSO (Sigma Aldrich) was added to control groups. ET-1 treatment lasted 24 h. For experiments that required transfection, cells were switched to starvation medium before transfection and treated with ET-1 24 h after transfection.

Plasmid construction

DNA fragments encoding the methyltransferases and catalytic mutants, and SYNPO2L isoforms, as well as fragments containing the *SYNPO2L* predicted promoter regions and putative DRE used in the luciferase assays, were purchased as gene fragments (Integrated DNA Technologies). The methyltransferase and SYNPO2L isoform fragments were cloned into the pcDNA3.1 expression vector. Promoter and regulatory-element fragments were cloned into the pGL4.23 luciferase reporter vector (Promega). All constructs were assembled using NEBuilder HiFi DNA Assembly (New England Biolabs). The plasmids generated in this study are available from the corresponding author upon reasonable request.

Transfection in hSC-CM

hSC-CMs were transfected with plasmids (500 ng per well in a 24-well plate) and 1 µl of Lipofectamine Stem Transfection Reagent (Thermo Fisher Scientific) according to the manufacturer's instructions. The culture medium was replaced 24 h after transfection.

qRT-PCR

Total RNA was reverse-transcribed with High-Capacity cDNA Reverse Transcription kit (Thermo Fisher Scientific). RNA expression levels were quantified using Taq Pro Universal SYBR qPCR Master Mix (Vazyme) and specific primers. qRT-PCR procedures were performed in accordance with the manufacturer's instructions. qRT-PCR data were analyzed using the delta-delta Ct method, with human/mouse *RPLPO* as the reference gene. Primer sequences are listed in Supplementary Table 8.

Western blotting

Proteins were extracted from the left ventricle using RIPA lysis buffer by TissueLyser III. Approximately 50 µg protein per sample was subjected to SDS–PAGE gel electrophoresis.

The primary antibodies used in this study were anti-METTL3 (Proteintech, 15073-1-AP, 1:1,000), anti-METTL14 (Sigma-Aldrich, HPA038002, 1:1,000), anti-WTAP (Proteintech, 10200-1-AP, 1:1,000), anti-METTL16 (Sigma-Aldrich, HPA020352, 1:1,000), anti-FTO (Proteintech, 27226-1-AP, 1:1,000), anti-ALKBH5 (Proteintech, 16837-1-AP, 1:1,000), anti-SYNPO2L (Proteintech, 21480-1-AP, 1:1,000) and anti-FLAG M2 (Sigma-Aldrich, F3165, 1:1,000). Protein expression levels were normalized to total protein using No-Stain Protein Labeling Reagent (Thermo Fisher Scientific). Full-length western blot membrane images are available in Source data.

Luciferase reporter assay

Luciferase reporter assay was performed in hSC-CMs with Dual-Luciferase Reporter Assay System (Promega) according to the manufacturer's instructions. Cells in 24-well plates were co-transfected with 450 ng pGL4.23 luciferase reporter vector and 50 ng pGL4.73 hRluc vector. Cells were lysed 48 h after transfection with 375 µl of Dual-Glo Reagent, and 150 µl mixed reagent was transferred to a 96-well-plate to measure firefly luminescence; 75 µl of Stop&Glo Reagent was then added to the 96-well-plate to measure Renilla luminescence. Reporter activity was calculated as the ratio of firefly to Renilla luminescence.

RNA methyltransferase perturbation

For RNA methyltransferase overexpression, hSC-CMs were transfected with the corresponding plasmids. Cells were collected 48 h after transfection. For pharmacologic inhibition of METTL3, hSC-CMs were treated with 5 µM STM2457 (TargetMol, T9060), while control groups received an equivalent volume of DMSO vehicle. Cells were incubated with STM2457 for 48 h. Where indicated, ET-1 was added 24 h following the initiation of STM2457.

MeRIP-qPCR

The enrichment of m^6A modified RNA was performed with EpiMark N6-Methyladenosine Enrichment Kit (NEB, E1610). Total RNA (≥5 µg) was fragmented using NEB RNA fragmentation buffer at 94 °C for 5 min, followed by immediate quenching with stop solution. Fragmented RNA was ethanol-precipitated and resuspended in water, and a 10% aliquot was saved as input. For immunoprecipitation, fragmented RNA was equally divided into two portions with one incubated with an anti-m^6A antibody or rabbit IgG control in 1× MeRIP IP buffer (10 mM Tris–HCl, 150 mM NaCl, 0.1% Igepal CA-630) supplemented with RNase inhibitor for 2 h at 4 °C with rotation. Recombinant protein A magnetic beads (Invitrogen, 10002D), pre-blocked with BSA, were added and incubated for an additional 2 h at 4 °C with rotation. Beads were washed five times with IP buffer, and m^6A-enriched RNA was eluted using free m^6A nucleoside. Eluted RNA was ethanol-precipitated, washed, air-dried and resuspended in water.

RNA enrichment was quantified by reverse transcription followed by qRT-PCR. For quality control, sample–primer pairs showing an IgG control threshold cycle (C_q) > 34 or undetermined values were confirmed to be free of nonspecific binding. Relative m^6A enrichment was determined by calculating the absolute percentage of input pulled down. To account for batch effects across independent MeRIP experiments, data were normalized to the vehicle control group (ET-1 -/ STM2457 -) and expressed as fold enrichment.

Actinomycin D mRNA stability assay

hSC-CMs were treated with 2 µM actinomycin D (Sigma-Aldrich, A9415) to block transcription at the onset of the assay. Fresh METTL3 inhibitor STM2457 was replenished in the medium of the treatment group at the time of actinomycin D administration. Cells were collected at baseline (0 h) and sequentially at 2 h, 4 h and 8 h after treatment for RNA extraction.

Relative mRNA abundance was quantified by reverse transcription followed by qRT-PCR. Relative mRNA abundance at each time point was normalized to the baseline initial value at $t = 0$ h ($Y = 1.0$). Nonlinear regression curve fitting was performed using a one-phase exponential decay model: $Y(t) = e^{-kt}$, where $Y(t)$ represents the relative fraction of remaining mRNA at time t (hours), and k denotes the first-order degradation rate constant (h^{-1}).

Statistical analyses

Results are presented as mean ± s.e.m. The name of the statistical test used is stated at the end of each figure legend. One-way analysis of variance (ANOVA) and unpaired two-tailed Student's t-test were performed using GraphPad Prism (v10.5.0). All other statistical tests

were performed using R software (v4.4.0). For bioinformatic analyses, the statistical parameters used in the pipelines of DGE, DMR, DTU and differential poly(A) tail length analyses are described in detail in their respective sections.

Reporting summary

Further information on research design is available in the Nature Portfolio Reporting Summary linked to this article.

Data availability

The data supporting the findings of this study are available from the corresponding author upon reasonable request. The m^{6}A basecalled bam files from ONT DRS have been deposited in the SRA database, BioProject ID PRJNA1348087.

References

1. Bozkurt, B. et al. Universal definition and classification of heart failure: a report of the Heart Failure Society of America, Heart Failure Association of the European Society of Cardiology, Japanese Heart Failure Society and Writing Committee of the Universal Definition of Heart Failure. *J. Card. Fail.* **27**, 387–413 https://doi.org/10.1016/j.cardfail.2021.01.022 (2021).
2. Harvey, P. A. & Leinwand, L. A. Cellular mechanisms of cardiomyopathy. *J. Cell Biol.* **194**, 355–365 (2011).
3. Seferović, P. M. et al. Heart failure in cardiomyopathies: a position paper from the Heart Failure Association of the European Society of Cardiology. *Eur. J. Heart Fail.* **21**, 553–576 (2019).
4. Rockman, H. A. et al. Segregation of atrial-specific and inducible expression of an atrial natriuretic factor transgene in an in vivo murine model of cardiac hypertrophy. *Proc. Natl Acad. Sci. USA* **88**, 8277–8281 https://doi.org/10.1073/pnas.88.18.8277 (1991).
5. Furihata, T. et al. The experimental model of transition from compensated cardiac hypertrophy to failure created by transverse aortic constriction in mice. *Int. J. Cardiol. Heart Vasc.* **11**, 24–28 https://doi.org/10.1016/j.ijcha.2016.03.007 (2016).
6. Richards, D. A. et al. Distinct phenotypes induced by three degrees of transverse aortic constriction in mice. *Sci. Rep.* **9**, 5844 https://doi.org/10.1038/s41598-019-42209-7 (2019).
7. Razeghi, P. et al. Metabolic gene expression in fetal and failing human heart. *Circulation* **104**, 2923–2931 (2001).
8. Porrello, E. R., Lee, C. J. M., Foo, R. S. Y. & Elliott, D. A. Transcriptional regulation in heart development, disease and regeneration: reassessing the fetal gene hypothesis. *Nat. Rev. Cardiol.* **23**, 183–196 https://doi.org/10.1038/s41569-025-01205-3 (2026).
9. Wang, C. et al. RNA modification in cardiovascular disease: implications for therapeutic interventions. *Signal Transduct. Target. Ther.* **8**, 412 https://doi.org/10.1038/s41392-023-01638-7 (2023).
10. Meyer, K. D. et al. Comprehensive analysis of mRNA methylation reveals enrichment in 3′ UTRs and near stop codons. *Cell* **149**, 1635–1646 (2012).
11. Wiener, D. & Schwartz, S. The epitranscriptome beyond m^{6}A. *Nat. Rev. Genet.* **22**, 119–131 https://doi.org/10.1038/s41576-020-00295-8 (2021).
12. Mathiyalagan, P. et al. FTO-dependent N^6-methyladenosine regulates cardiac function during remodeling and repair. *Circulation* **139**, 518–532 https://doi.org/10.1161/CIRCULATIONAHA.118.033794 (2019).
13. Dorn, L. E. et al. The N^6-methyladenosine mRNA methylase METTL3 controls cardiac homeostasis and hypertrophy. *Circulation* **139**, 533–545 https://doi.org/10.1161/CIRCULATIONAHA.118.036146 (2019).
14. Hinger, S. A. et al. Remodeling of the m^{6}A landscape in the heart reveals few conserved post-transcriptional events underlying cardiomyocyte hypertrophy. *J. Mol. Cell. Cardiol.* **151**, 46–55 https://doi.org/10.1016/j.yjmcc.2020.11.002 (2021).
15. Li, W. et al. Comprehensive analysis of RNA m^{6}A methylation in pressure overload-induced cardiac hypertrophy. *BMC Genomics* **23**, 576 https://doi.org/10.1186/s12864-022-08833-w (2022).
16. Kmietczyk, V. et al. m6A-mRNA methylation regulates cardiac gene expression and cellular growth. *Life Sci. Alliance* **2** https://doi.org/10.26508/lsa.201800233 (2019).
17. Dominissini, D. et al. Topology of the human and mouse m^{6}A RNA methylomes revealed by m^{6}A-seq. *Nature* **485**, 201–206 https://doi.org/10.1038/nature11112 (2012).
18. Linder, B. et al. Single-nucleotide-resolution mapping of m^{6}A and m^{6}Am throughout the transcriptome. *Nat. Methods* **12**, 767–772 https://doi.org/10.1038/nmeth.3453 (2015).
19. Jain, M., Abu-Shumays, R., Olsen, H. E. & Akeson, M. Advances in nanopore direct RNA sequencing. *Nat. Methods* **19**, 1160–1164 (2022).
20. Garalde, D. R. et al. Highly parallel direct RNA sequencing on an array of nanopores. *Nat. Methods* **15**, 201–206 https://doi.org/10.1038/nmeth.4577 (2018).
21. Pratanwanich, P. N. et al. Identification of differential RNA modifications from nanopore direct RNA sequencing with xPore. *Nat. Biotechnol.* **39**, 1394–1402 https://doi.org/10.1038/s41587-021-00949-w (2021).
22. Kim, Y. et al. Nanopore direct RNA sequencing of human transcriptomes reveals the complexity of mRNA modifications and crosstalk between regulatory features. *Cell Genomics* **5**, 100872 https://doi.org/10.1016/j.xgen.2025.100872 (2025).
23. Lorenz, D. A., Sathe, S., Einstein, J. M. & Yeo, G. W. Direct RNA sequencing enables m^{6}A detection in endogenous transcript isoforms at base-specific resolution. *RNA* **26**, 19–28 (2020).
24. Yang, Y., Hsu, P. J., Chen, Y.-S. & Yang, Y.-G. Dynamic transcriptomic m^{6}A decoration: writers, erasers, readers and functions in RNA metabolism. *Cell Res.* **28**, 616–624 https://doi.org/10.1038/s41422-018-0040-8 (2018).
25. Zhu, Z. M., Huo, F. C., Zhang, J., Shan, H. J. & Pei, D. S. Crosstalk between m^{6}A modification and alternative splicing during cancer progression. *Clin. Transl. Med.* **13**, e1460 https://doi.org/10.1002/ctm2.1460 (2023).
26. Reyes, A. & Huber, W. Alternative start and termination sites of transcription drive most transcript isoform differences across human tissues. *Nucleic Acids Res.* **46**, 582–592 https://doi.org/10.1093/nar/gkx1165 (2018).
27. Molinie, B. et al. m(6)A-LAIC-seq reveals the census and complexity of the m(6)A epitranscriptome. *Nat. Methods* **13**, 692–698 https://doi.org/10.1038/nmeth.3898 (2016).
28. Gleeson, J. et al. Isoform-level profiling of m(6)A epitranscriptomic signatures in human brain. *Sci. Adv.* **11**, eadp0783 https://doi.org/10.1126/sciadv.adp0783 (2025).
29. Shachar, R. et al. Dissecting the sequence and structural determinants guiding m^{6}A deposition and evolution via inter- and intra-species hybrids. *Genome Biol.* **25**, 48 https://doi.org/10.1186/s13059-024-03182-1 (2024).
30. Hofacker, I. L. Vienna RNA secondary structure server. *Nucleic Acids Res.* **31**, 3429–3431 https://doi.org/10.1093/nar/gkg599 (2003).
31. Lizio, M. et al. Gateways to the FANTOM5 promoter level mammalian expression atlas. *Genome Biol.* **16**, 22 https://doi.org/10.1186/s13059-014-0560-6 (2015).
32. Redwanz, C. et al. Endothelin-1 influences mechanical properties and contractility of hiPSC derived cardiomyocytes resulting in diastolic dysfunction. *J. Mol. Cell. Cardiol.* **194**, 105–117 https://doi.org/10.1016/j.yjmcc.2024.07.004 (2024).
33. Moore, J. E. et al. An expanded registry of candidate *cis*-regulatory elements. *Nature* https://doi.org/10.1038/s41586-025-09909-9 (2026).

34. Murray, C. S. et al. Integration of dilated cardiomyopathy genomics with transcriptomics from the human heart implicates regulatory molecular mechanisms. Preprint at *medRxiv* https://doi.org/10.64898/2026.01.12.26343934 (2026).
35. Wang, P., Doxtader, K. A. & Nam, Y. Structural basis for cooperative function of Mettl3 and Mettl14 methyltransferases. *Mol. Cell* **63**, 306–317 https://doi.org/10.1016/j.molcel.2016.05.041 (2016).
36. Esfahani, N. G., Stein, A. J., Akeson, S., Tzadikario, T. & Jain, M. Evaluation of Nanopore direct RNA sequencing updates for modification detection. Preprint at *bioRxiv* https://doi.org/10.1101/2025.05.01.651717 (2025).
37. Rabolli, C. P. et al. Nanopore detection of METTL3-dependent m^{6}A-modified mRNA reveals a new mechanism regulating cardiomyocyte mitochondrial metabolism. *Circulation* **149**, 1319–1322 https://doi.org/10.1161/CIRCULATIONAHA.123.066473 (2024).
38. Du, H. et al. YTHDF2 destabilizes m^{6}A-containing RNA through direct recruitment of the CCR4–NOT deadenylase complex. *Nat. Commun.* **7**, 12626 https://doi.org/10.1038/ncomms12626 (2016).
39. Huang, H. et al. Recognition of RNA N(6)-methyladenosine by IGF2BP proteins enhances mRNA stability and translation. *Nat. Cell Biol.* **20**, 285–295 https://doi.org/10.1038/s41556-018-0045-z (2018).
40. Wang, X. et al. N^6-methyladenosine-dependent regulation of messenger RNA stability. *Nature* **505**, 117–120 https://doi.org/10.1038/nature12730 (2014).
41. Wen, S. et al. Long non-coding RNA NEAT1 promotes bone metastasis of prostate cancer through N^6-methyladenosine. *Mol. Cancer* **19**, 171 (2020).
42. Mamontova, V. et al. NEAT1 promotes genome stability via m^{6}A methylation-dependent regulation of CHD4. *Genes Dev.* **38**, 915–930 (2024).
43. Pu, X., Gu, Z. & Gu, Z. ALKBH5 regulates IGF1R expression to promote the proliferation and tumorigenicity of endometrial cancer. *J. Cancer* **11**, 5612–5622 (2020).
44. Wu, J. et al. METTL16 promotes stability of SYNPO2L mRNA and leading to cancer cell lung metastasis by secretion of COL10A1 and attract the cancer-associated fibroblasts. *Int. J. Biol. Sci.* **20**, 4128–4145 (2024).
45. Clausen, A. G., Vad, O. B., Andersen, J. H. & Olesen, M. S. Loss-of-function variants in the SYNPO2L gene are associated with atrial fibrillation. *Front. Cardiovasc. Med.* **8**, 650667 (2021).
46. Beqqali, A. et al. CHAP is a newly identified Z-disc protein essential for heart and skeletal muscle function. *J. Cell Sci.* **123**, 1141–1150 https://doi.org/10.1242/jcs.063859 (2010).
47. Wass, S. Y. et al. Transcriptomic insights into the atrial fibrillation susceptibility locus near the MYOZ1 and SYNPO2L genes. *Int. J. Mol. Sci.* **25**, 10309 (2024).
48. Lee, W. L. et al. An RNA modification enzyme directly senses reactive oxygen species for translational regulation in *Enterococcus faecalis*. *Nat. Commun.* **14**, 4093 https://doi.org/10.1038/s41467-023-39790-x (2023).
49. Chen, Y. et al. Context-aware transcript quantification from long-read RNA-seq data with Bambu. *Nat. Methods* **20**, 1187–1195 https://doi.org/10.1038/s41592-023-01908-w (2023).
50. Love, M., Anders, S. & Huber, W. Differential analysis of count data–the DESeq2 package. *Genome Biol.* **15**, 10–1186 (2014).
51. Ashburner, M. et al. Gene ontology: tool for the unification of biology. The Gene Ontology Consortium. *Nat. Genet.* **25**, 25–29 https://doi.org/10.1038/75556 (2000).
52. Aleksander, S. A. et al. The Gene Ontology knowledgebase in 2023. *Genetics* **224**, iyad031 https://doi.org/10.1093/genetics/iyad031 (2023).
53. Love, M. I., Soneson, C. & Patro, R. Swimming downstream: statistical analysis of differential transcript usage following Salmon quantification. *F1000Res.* **7**, 952 https://doi.org/10.12688/f1000research.15398.3 (2018).
54. Sun, H. et al. Mild and ultrafast GLORI enables absolute quantification of m^{6}A methylome from low-input samples. *Nat. Methods* **22**, 1226–1236 https://doi.org/10.1038/s41592-025-02680-9 (2025).
55. Lee, C. J. M. et al. Genome-wide CRISPR screen identifies an NF2-adherens junction mechanistic dependency for cardiac lineage. *Circulation* **149**, 1960–1979 https://doi.org/10.1161/circulationaha.122.061335 (2024).
56. Robinson, J. T. et al. Integrative genomics viewer. *Nat. Biotechnol.* **29**, 24–26 https://doi.org/10.1038/nbt.1754 (2011).
57. Casper, J. et al. The UCSC Genome Browser database: 2026 update. *Nucleic Acids Res.* **54**, D1331–D1335 https://doi.org/10.1093/nar/gkaf1250 (2026).

Acknowledgements

We thank M. Ackers-Johnson, P. Vidyasekar and H. Yang at the National University of Singapore for their advice in experiment design and technical skills. We thank R. Kramann at RWTH Aachen University Hospital for providing the iPS cell line 353. We thank C. Ying at A*STAR GIS for her help in using Bambu.

Author contributions

Z.X. and R.S.Y.F. conceived the project, designed the experiments and wrote the article. Z.X. conducted the wet laboratory experiments. Z.X. and C.T. performed the sequencing data analysis. J.W.C., C.J.M.L., W.T., G.L.Q.T., R.Q. and Z.T. offered support in wet laboratory experiments. D.G.R.Y. and L.C. performed LC–MS/MS. L.D.A.T. performed animal experiments. J.M.A., V.T. and C.J.M.L. provided materials and resources.

Funding

R.S.Y.F. is supported by grants from the Singapore Ministry of Health's National Medical Research Council under the Clinician Scientist-Individual Research Grant (CS-IRG—MOH-001480-00, MOH-001325-00, MOH-001699), Clinician Scientist-Senior Investigator (CSA-SI—MOH-001685), Open Fund-Large Collaborative Grant (MOH-001226-00) and Ministry of Education (MOH-000333-00) and by the RIE2020/RIE2025 PREVENT-HF Industry Alignment Fund Pre-Positioning Programme (IAF-PP H23J2a0033), administered by A*STAR. Z.X. is supported by grants from the Singapore Ministry of Education under M2CardAGE grant (MOET32021-0003) and the Research Scholarship at Yong Loo Lin School of Medicine, National University of Singapore. C.J.M.L. is supported by grants from the Singapore Ministry of Health's National Medical Research Council under the Young Investigator Research Grant (MOH-001712-00). V.T. is supported by grants from the Agency for Science, Technology and Research (A*STAR), the National Research Foundation (NRF) Singapore (NRF-CRP26-2021-0001).

Competing interests

The authors declare no competing interests.

Additional information

Extended data is available for this paper at https://doi.org/10.1038/s44161-026-00898-0.

Supplementary information The online version contains supplementary material available at https://doi.org/10.1038/s44161-026-00898-0.

Correspondence and requests for materials should be addressed to Roger S. Y. Foo.

Peer review information *Nature Cardiovascular Research* thanks Christoph Dieterich, and the other, anonymous, reviewer(s) for their contribution to the peer review of this work.

Reprints and permissions information is available at www.nature.com/reprints.

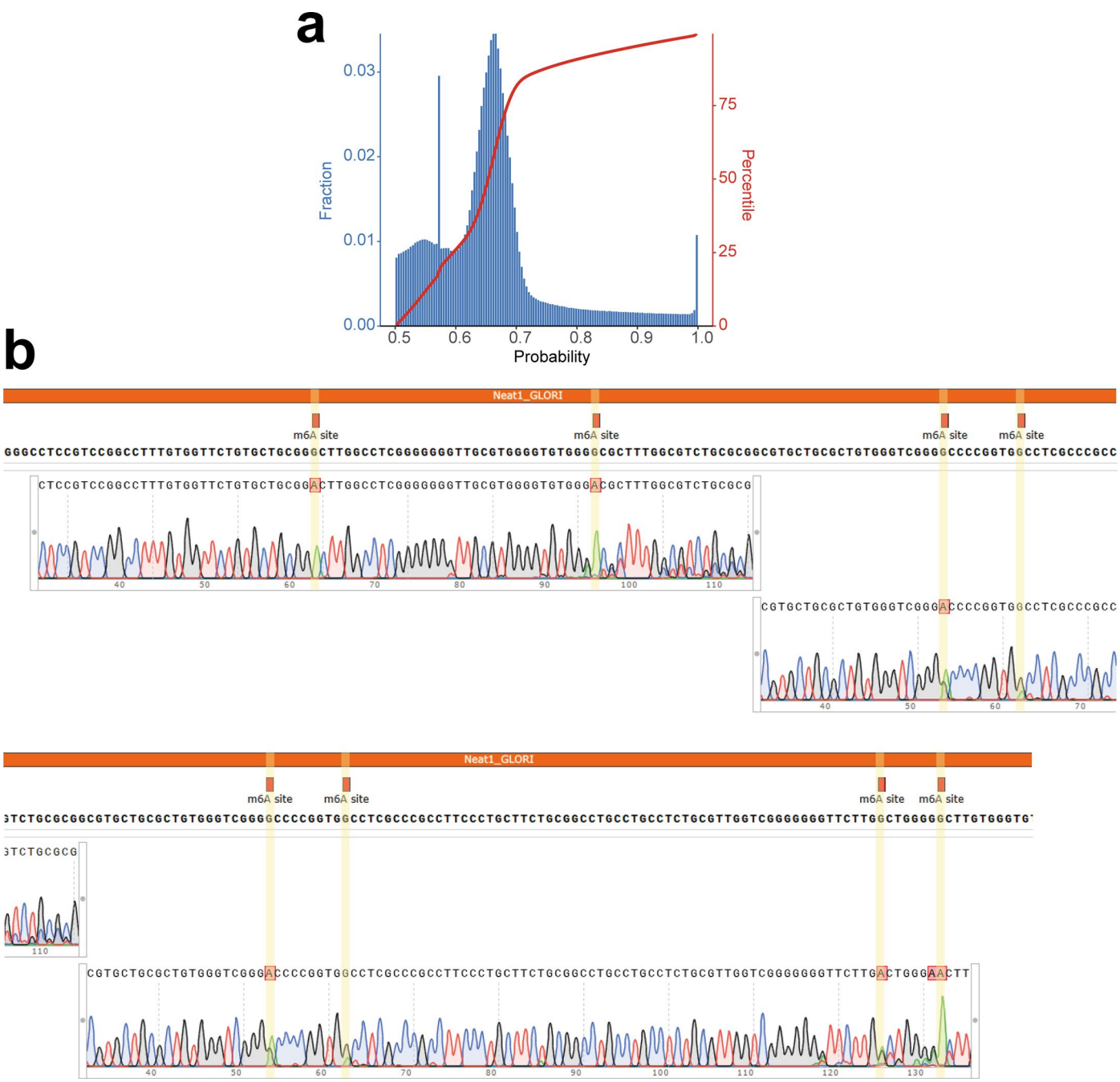
Publisher's note Springer Nature remains neutral with regard to jurisdictional claims in published maps and institutional affiliations.

Open Access This article is licensed under a Creative Commons Attribution-NonCommercial-NoDerivatives 4.0 International License, which permits any non-commercial use, sharing, distribution and reproduction in any medium or format, as long as you give appropriate credit to the original author(s) and the source, provide a link to the Creative Commons licence, and indicate if you modified the licensed material. You do not have permission under this licence to share adapted material derived from this article or parts of it. The images or other third party material in this article are included in the article's Creative Commons licence, unless indicated otherwise in a credit line to the material. If material is not included in the article's Creative Commons licence and your intended use is not permitted by statutory regulation or exceeds the permitted use, you will need to obtain permission directly from the copyright holder. To view a copy of this licence, visit http://creativecommons.org/licenses/by-nc-nd/4.0/.

© The Author(s) 2026

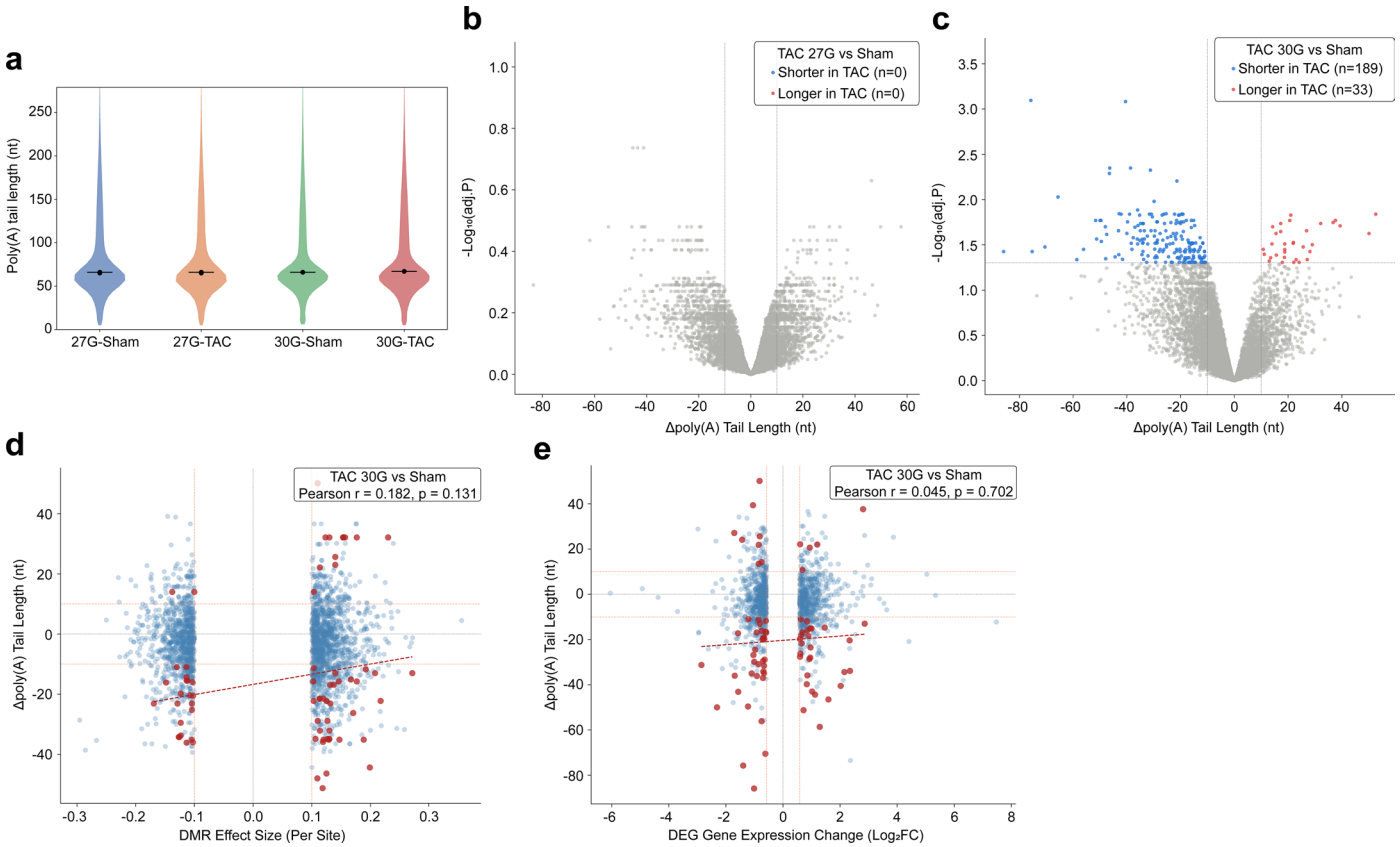
[1]Cardiovascular-Metabolic Disease Translational Research Programme, Yong Loo Lin School of Medicine, National University of Singapore, Singapore, Singapore. [2]Department of Pharmacy and Pharmaceutical Sciences, Faculty of Science, National University of Singapore, Singapore, Singapore. [3]Institute of Molecular and Cell Biology, A*STAR, Singapore, Singapore. [4]Department of Medicine, Yong Loo Lin School of Medicine, National University of Singapore, Singapore, Singapore. [5]Singapore-MIT Alliance for Research & Technology, Singapore, Singapore. [6]Center for Cardiovascular Research, Division of Cardiology, Department of Medicine, Washington University School of Medicine, Saint Louis, MO, USA. [7]Helmholtz-Institute for Translational AngioCardioScience (HI-TAC) of the Max Delbrück Center at Heidelberg University, Heidelberg, Germany. [8]Department of Biochemistry, Yong Loo Lin School of Medicine, National University of Singapore, Singapore, Singapore. [9]FSCPO: Ministry of Education Frontiers Science Center for Precision Oncology, University of Macau, Macao, China. [10]Cancer Center, Faculty of Health Sciences, University of Macau, Macao, China. ✉e-mail: roger.foo@nus.edu.sg

https://doi.org/10.1038/s44161-026-00898-0



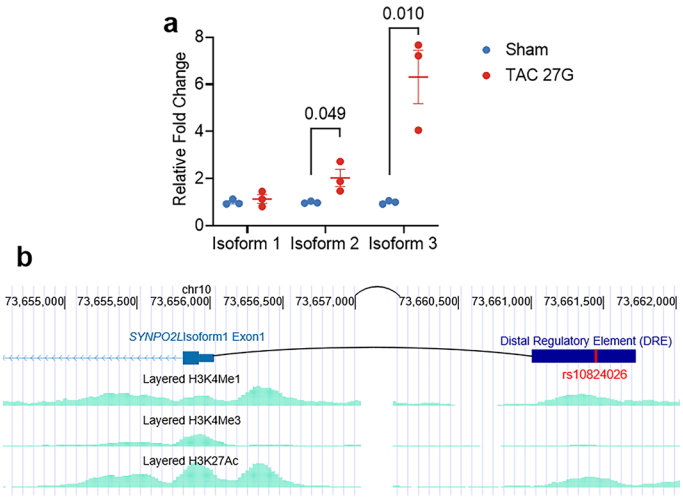
Extended Data Fig. 1 | DRS model and GLORI validation. a, Dual-axis plots of base modification probability of m^{6}A calls by random context Dorado m^{6}A basecalling model. **b**, GLORI detection of m^{6}A sites in transcript *Neat1*, showing the original sequence (first row), predicted GLORI-treated sequence (second row) and sequencing result with chromatogram (third row).

https://doi.org/10.1038/s44161-026-00898-0



Extended Data Fig. 2 | Differential poly(A) tail length analysis. a, Violin plots of the global distribution of poly(A) tail lengths across the TAC 27 G vs sham and TAC 30 G vs sham datasets. **b**–**c**, Volcano plots of transcript-level poly(A) tail length changes for TAC 27 G **(b)** and TAC 30 G **(c)** datasets. **d**, Scatter plot of site-level correlations between differential poly(A) tail length changes and DMR effect sizes in the TAC 30 G dataset. Each point represents a DMR site paired with its corresponding poly(A) tail length change. Red points represent the poly(A) tail length change of the pairs met the thresholds, while blue points represent those did not meet the thresholds. The dashed red line shows the linear regression fit of the red points, with the corresponding Pearson's correlation coefficient (r) and p-value provided. **e**, Scatter plot of gene-level correlations between differential poly(A) tail length changes and DEG gene expression changes in the TAC 30 G dataset. Each point represents a gene (log2FC >|0.58 |) paired with its corresponding poly(A) tail length change. Red points represent the poly(A) tail length change of the pairs met the thresholds, while blue points represent those did not meet the thresholds. The dashed red line shows the linear regression fit of the red points, with the corresponding Pearson's correlation coefficient (r) and p-value provided. Statistical tests for Differential Poly(A) tail length analysis (**b**,**c**) are described in the Methods and P values were adjusted using the Benjamini–Hochberg procedure, or carried out by using two-sided Pearson correlation analysis (**d**, **e**).

https://doi.org/10.1038/s44161-026-00898-0



Extended Data Fig. 3 | *Synpo2l* expression and DRE identification. a, Relative fold change of each *Synpo2l* isoform by qRT-PCR in sham versus TAC 27 G ($n = 3$ for each group). **b**, Putative DRE region of *SYNPO2L* on the human genome, with the reported sQTL rs10824026 annotated. Tracks of histone modifications (H3K4Me1, H3K4Me3, and H3K27Ac) in HSMM (human skeletal muscle myoblast) cells from ENCODE are shown, retrieved from the UCSC Genome Browser. Data are shown as mean ± s.e.m. p-values are annotated to show statistical significance. Statistics carried out by using unpaired two-tailed Student's *t*-test (**a**).

nature portfolio

Corresponding author(s): Roger S. Y. Foo

Last updated by author(s): Sep 18, 2026

Reporting Summary

Nature Portfolio wishes to improve the reproducibility of the work that we publish. This form provides structure for consistency and transparency in reporting. For further information on Nature Portfolio policies, see our Editorial Policies and the Editorial Policy Checklist.

Statistics

For all statistical analyses, confirm that the following items are present in the figure legend, table legend, main text, or Methods section.

n/a	Confirmed	
☐	☒	The exact sample size (*n*) for each experimental group/condition, given as a discrete number and unit of measurement
☐	☒	A statement on whether measurements were taken from distinct samples or whether the same sample was measured repeatedly
☐	☒	The statistical test(s) used AND whether they are one- or two-sided *Only common tests should be described solely by name; describe more complex techniques in the Methods section.*
☒	☐	A description of all covariates tested
☐	☒	A description of any assumptions or corrections, such as tests of normality and adjustment for multiple comparisons
☐	☒	A full description of the statistical parameters including central tendency (e.g. means) or other basic estimates (e.g. regression coefficient) AND variation (e.g. standard deviation) or associated estimates of uncertainty (e.g. confidence intervals)
☐	☒	For null hypothesis testing, the test statistic (e.g. *F*, *t*, *r*) with confidence intervals, effect sizes, degrees of freedom and *P* value noted *Give P values as exact values whenever suitable.*
☒	☐	For Bayesian analysis, information on the choice of priors and Markov chain Monte Carlo settings
☒	☐	For hierarchical and complex designs, identification of the appropriate level for tests and full reporting of outcomes
☐	☒	Estimates of effect sizes (e.g. Cohen's *d*, Pearson's *r*), indicating how they were calculated

Our web collection on statistics for biologists contains articles on many of the points above.

Software and code

Policy information about availability of computer code

Data collection	MinKNOW (v25.03.7), Dorado (v1.0.0) for sequencing data, iBright FL1000 for WB data, QuantStudio 5 for qPCR data, Tecan i-control for luciferase assay
Data analysis	Bambu (v3.2.4), DESeq2 (v1.46.0), Modkit (v0.4.2), DRIMSeq (v1.34.0), DEXSeq (v1.52.0), stageR (v1.28.0), GenomicRanges (v1.58.0) and rtracklayer (v1.66.0) for sequencing data, Vevo LAB (v1.7.1) for echocardiography data, imagej (1.54g) for WB data, GraphPad Prism (v10.5.0) and R (v4.4.0) for data statistical analysis

For manuscripts utilizing custom algorithms or software that are central to the research but not yet described in published literature, software must be made available to editors and reviewers. We strongly encourage code deposition in a community repository (e.g. GitHub). See the Nature Portfolio guidelines for submitting code & software for further information.

Data

Policy information about availability of data

All manuscripts must include a data availability statement. This statement should provide the following information, where applicable:

- Accession codes, unique identifiers, or web links for publicly available datasets
- A description of any restrictions on data availability
- For clinical datasets or third party data, please ensure that the statement adheres to our policy

The data supporting the findings of this study are available from the corresponding authors upon reasonable request. The m6A basecalled bam files from ONT DRS have been deposited in the SRA database, BioProject ID PRJNA1348087.

Research involving human participants, their data, or biological material

Policy information about studies with human participants or human data. See also policy information about sex, gender (identity/presentation), and sexual orientation and race, ethnicity and racism.

Reporting on sex and gender	In this study, only biopsy specimens from DCM patients and healthy donors were used. Sex and gender information was not collected.
Reporting on race, ethnicity, or other socially relevant groupings	NA
Population characteristics	NA
Recruitment	NA
Ethics oversight	Study protocols for the collection and use of human cardiac tissue for research were approved (Approval Number L12-405) by the National University of Singapore institutional review board committee, in accordance with its guidelines and supervision. All experiments performed with human embryonic stem cells (hESCs) were conducted in accordance with the guidelines and under the supervision of the National University of Singapore institutional review board committee (Approval Number NUS-IRB-2024-810). Generation and use of the induced pluripotent stem cell (iPSC) line 353 were approved by the ethics commission at RWTH Aachen University Hospital (approval number EK206/09).

Note that full information on the approval of the study protocol must also be provided in the manuscript.

Field-specific reporting

Please select the one below that is the best fit for your research. If you are not sure, read the appropriate sections before making your selection.

☒ Life sciences ☐ Behavioural & social sciences ☐ Ecological, evolutionary & environmental sciences

For a reference copy of the document with all sections, see nature.com/documents/nr-reporting-summary-flat.pdf

Life sciences study design

All studies must disclose on these points even when the disclosure is negative.

Sample size	A total of 8 mice per group were selected for surgery, based on prior experience with surgical success rates and expected perioperative mortality. After surgery, sample sizes of n = 3–4 per group were determined according to sample availability while maintaining adequate statistical power for downstream analysis. For other wet lab experiments, sample sizes of n = 4 per group were determined according to sample availability while maintaining adequate statistical power for downstream analysis.
Data exclusions	Exclusion criteria were defined prior to surgery based on previous experimental experience. Mice that died within 4 weeks after surgery or failed for transverse aortic constriction due to surgical variability were excluded from analysis. Specifically, 5 mice were excluded from the TAC 27G group and 4 mice from the TAC 30G group. For other wet lab experiments, no data generated were excluded.
Replication	All experiments included at least three independent biological replicates. Exact sample sizes and the definitions of biological replicates are provided in the corresponding figure legends and Source Data.
Randomization	Mice were genetically identical and randomly assigned to surgery and control groups. No formal randomization procedure was used for cell-culture experiments; treatments were applied to parallel cultures derived from the same cell preparation.
Blinding	Investigators were blinded to surgical group allocation during echocardiographic assessment and sample collection. Group information was

Blinding	unblinded prior to sequencing and subsequent wet-lab experiments to enable appropriate sample handling and analysis. Cell-culture experiments were not performed under blinded conditions; data were acquired using quantitative experimental readouts.

Reporting for specific materials, systems and methods

We require information from authors about some types of materials, experimental systems and methods used in many studies. Here, indicate whether each material, system or method listed is relevant to your study. If you are not sure if a list item applies to your research, read the appropriate section before selecting a response.

Materials & experimental systems

n/a	Involved in the study
☐	☒ Antibodies
☐	☒ Eukaryotic cell lines
☐	☐ Palaeontology and archaeology
☐	☒ Animals and other organisms
☐	☐ Clinical data
☐	☐ Dual use research of concern
☐	☐ Plants

Methods

n/a	Involved in the study
☐	☐ ChIP-seq
☐	☐ Flow cytometry
☐	☐ MRI-based neuroimaging

Antibodies

Antibodies used	Anti-METTL3 (Proteintech, 15073-1-AP), anti-METTL14 (Sigma-Aldrich, HPA038002), anti-WTAP (Proteintech, 10200-1-AP), anti-METTL16 (Sigma-Aldrich, HPA020352), anti-FTO (Proteintech, 27226-1-AP), anti-ALKBH5 (Proteintech, 16837-1-AP), anti-SYNPO2L (Proteintech, 21480-1-AP) and anti-FLAG M2 (Sigma-Aldrich, F3165). HRP-conjugated Goat Anti-Mouse IgG(H+L) (Proteintech, SA00001-1), HRP-conjugated Goat Anti-Rabbit IgG(H+L) (Proteintech, SA00001-2). All primary antibodies used for WB were diluted 1:1000, all secondary antibodies used for WB were diluted 1:5000.
Validation	All antibodies were validated by the manufacturer for the specified applications, based on manufacturer websites.

Eukaryotic cell lines

Policy information about cell lines and Sex and Gender in Research

Cell line source(s)	H1 embryonic stem cell line (WA01, WiCell), HEK293T cell line (CRL-3216, ATCC), iPS cell-353 line was generated from the erythroblasts cells of a healthy male volunteer (40y) after informed consent. Human iPSC cell culture was approved by the ethics committee of the Medical Faculty of RWTH Aachen University (EK206/09).
Authentication	H1 hESCs and HEK293T cells were not authenticated. For iPSC-353, the validation is performed by Erasmus MC iPS core facility.
Mycoplasma contamination	All cell lines tested negative for mycoplasma.
Commonly misidentified lines (See ICLAC register)	*Name any commonly misidentified cell lines used in the study and provide a rationale for their use.*

Palaeontology and Archaeology

Specimen provenance	*Provide provenance information for specimens and describe permits that were obtained for the work (including the name of the issuing authority, the date of issue, and any identifying information). Permits should encompass collection and, where applicable, export.*
Specimen deposition	*Indicate where the specimens have been deposited to permit free access by other researchers.*
Dating methods	*If new dates are provided, describe how they were obtained (e.g. collection, storage, sample pretreatment and measurement), where they were obtained (i.e. lab name), the calibration program and the protocol for quality assurance OR state that no new dates are provided.*

☐ Tick this box to confirm that the raw and calibrated dates are available in the paper or in Supplementary Information.

Ethics oversight	*Identify the organization(s) that approved or provided guidance on the study protocol, OR state that no ethical approval or guidance was required and explain why not.*

Note that full information on the approval of the study protocol must also be provided in the manuscript.

Animals and other research organisms

Policy information about studies involving animals; ARRIVE guidelines recommended for reporting animal research, and Sex and Gender in Research

Laboratory animals	C57BL/6J mice of 8 week old
Wild animals	The study did not involve wild animals.
Reporting on sex	Only male mice were used to minimize variability arising from hormonal cycles and to ensure consistency with previous studies of the transverse aortic constriction heart failure model. Sex was therefore not considered a biological variable in this study.
Field-collected samples	The study did not involve field-collected samples.
Ethics oversight	All animal experimental procedures were approved by the National University of Singapore institutional animal care and use committee and undertaken in strict accordance with the Singapore National Advisory Committee for Laboratory Animal Research guidelines.

Note that full information on the approval of the study protocol must also be provided in the manuscript.

Clinical data

Policy information about clinical studies

All manuscripts should comply with the ICMJE guidelines for publication of clinical research and a completed CONSORT checklist must be included with all submissions.

Clinical trial registration	*Provide the trial registration number from ClinicalTrials.gov or an equivalent agency.*
Study protocol	*Note where the full trial protocol can be accessed OR if not available, explain why.*
Data collection	*Describe the settings and locales of data collection, noting the time periods of recruitment and data collection.*
Outcomes	*Describe how you pre-defined primary and secondary outcome measures and how you assessed these measures.*

Dual use research of concern

Policy information about dual use research of concern

Hazards

Could the accidental, deliberate or reckless misuse of agents or technologies generated in the work, or the application of information presented in the manuscript, pose a threat to:

No	Yes	
☐	☐	Public health
☐	☐	National security
☐	☐	Crops and/or livestock
☐	☐	Ecosystems
☐	☐	Any other significant area

Experiments of concern

Does the work involve any of these experiments of concern:

No	Yes	
☐	☐	Demonstrate how to render a vaccine ineffective
☐	☐	Confer resistance to therapeutically useful antibiotics or antiviral agents
☐	☐	Enhance the virulence of a pathogen or render a nonpathogen virulent
☐	☐	Increase transmissibility of a pathogen
☐	☐	Alter the host range of a pathogen
☐	☐	Enable evasion of diagnostic/detection modalities
☐	☐	Enable the weaponization of a biological agent or toxin
☐	☐	Any other potentially harmful combination of experiments and agents

Plants

Seed stocks — *Report on the source of all seed stocks or other plant material used. If applicable, state the seed stock centre and catalogue number. If plant specimens were collected from the field, describe the collection location, date and sampling procedures.*

Novel plant genotypes — *Describe the methods by which all novel plant genotypes were produced. This includes those generated by transgenic approaches, gene editing, chemical/radiation-based mutagenesis and hybridization. For transgenic lines, describe the transformation method, the number of independent lines analyzed and the generation upon which experiments were performed. For gene-edited lines, describe the editor used, the endogenous sequence targeted for editing, the targeting guide RNA sequence (if applicable) and how the editor was applied.*

Authentication — *Describe any authentication procedures for each seed stock used or novel genotype generated. Describe any experiments used to assess the effect of a mutation and, where applicable, how potential secondary effects (e.g. second site T-DNA insertions, mosiacism, off-target gene editing) were examined.*

ChIP-seq

Data deposition

☐ Confirm that both raw and final processed data have been deposited in a public database such as GEO.

☐ Confirm that you have deposited or provided access to graph files (e.g. BED files) for the called peaks.

Data access links
May remain private before publication. — *For "Initial submission" or "Revised version" documents, provide reviewer access links. For your "Final submission" document, provide a link to the deposited data.*

Files in database submission — *Provide a list of all files available in the database submission.*

Genome browser session
(e.g. UCSC) — *Provide a link to an anonymized genome browser session for "Initial submission" and "Revised version" documents only, to enable peer review. Write "no longer applicable" for "Final submission" documents.*

Methodology

Replicates — *Describe the experimental replicates, specifying number, type and replicate agreement.*

Sequencing depth — *Describe the sequencing depth for each experiment, providing the total number of reads, uniquely mapped reads, length of reads and whether they were paired- or single-end.*

Antibodies — *Describe the antibodies used for the ChIP-seq experiments; as applicable, provide supplier name, catalog number, clone name, and lot number.*

Peak calling parameters — *Specify the command line program and parameters used for read mapping and peak calling, including the ChIP, control and index files used.*

Data quality — *Describe the methods used to ensure data quality in full detail, including how many peaks are at FDR 5% and above 5-fold enrichment.*

Software — *Describe the software used to collect and analyze the ChIP-seq data. For custom code that has been deposited into a community repository, provide accession details.*

Flow Cytometry

Plots

Confirm that:

☐ The axis labels state the marker and fluorochrome used (e.g. CD4-FITC).

☐ The axis scales are clearly visible. Include numbers along axes only for bottom left plot of group (a 'group' is an analysis of identical markers).

☐ All plots are contour plots with outliers or pseudocolor plots.

☐ A numerical value for number of cells or percentage (with statistics) is provided.

Methodology

Sample preparation — *Describe the sample preparation, detailing the biological source of the cells and any tissue processing steps used.*

Instrument — *Identify the instrument used for data collection, specifying make and model number.*

Software — *Describe the software used to collect and analyze the flow cytometry data. For custom code that has been deposited into a community repository, provide accession details.*

Cell population abundance

Describe the abundance of the relevant cell populations within post-sort fractions, providing details on the purity of the samples and how it was determined.

Gating strategy

Describe the gating strategy used for all relevant experiments, specifying the preliminary FSC/SSC gates of the starting cell population, indicating where boundaries between "positive" and "negative" staining cell populations are defined.

☐ Tick this box to confirm that a figure exemplifying the gating strategy is provided in the Supplementary Information.

Magnetic resonance imaging

Experimental design

Design type

Indicate task or resting state; event-related or block design.

Design specifications

Specify the number of blocks, trials or experimental units per session and/or subject, and specify the length of each trial or block (if trials are blocked) and interval between trials.

Behavioral performance measures

State number and/or type of variables recorded (e.g. correct button press, response time) and what statistics were used to establish that the subjects were performing the task as expected (e.g. mean, range, and/or standard deviation across subjects).

Acquisition

Imaging type(s)

Specify: functional, structural, diffusion, perfusion.

Field strength

Specify in Tesla

Sequence & imaging parameters

Specify the pulse sequence type (gradient echo, spin echo, etc.), imaging type (EPI, spiral, etc.), field of view, matrix size, slice thickness, orientation and TE/TR/flip angle.

Area of acquisition

State whether a whole brain scan was used OR define the area of acquisition, describing how the region was determined.

Diffusion MRI ☐ Used ☐ Not used

Preprocessing

Preprocessing software

Provide detail on software version and revision number and on specific parameters (model/functions, brain extraction, segmentation, smoothing kernel size, etc.).

Normalization

If data were normalized/standardized, describe the approach(es): specify linear or non-linear and define image types used for transformation OR indicate that data were not normalized and explain rationale for lack of normalization.

Normalization template

Describe the template used for normalization/transformation, specifying subject space or group standardized space (e.g. original Talairach, MNI305, ICBM152) OR indicate that the data were not normalized.

Noise and artifact removal

Describe your procedure(s) for artifact and structured noise removal, specifying motion parameters, tissue signals and physiological signals (heart rate, respiration).

Volume censoring

Define your software and/or method and criteria for volume censoring, and state the extent of such censoring.

Statistical modeling & inference

Model type and settings

Specify type (mass univariate, multivariate, RSA, predictive, etc.) and describe essential details of the model at the first and second levels (e.g. fixed, random or mixed effects; drift or auto-correlation).

Effect(s) tested

Define precise effect in terms of the task or stimulus conditions instead of psychological concepts and indicate whether ANOVA or factorial designs were used.

Specify type of analysis: ☐ Whole brain ☐ ROI-based ☐ Both

Statistic type for inference

Specify voxel-wise or cluster-wise and report all relevant parameters for cluster-wise methods.

(See Eklund et al. 2016)

Correction

Describe the type of correction and how it is obtained for multiple comparisons (e.g. FWE, FDR, permutation or Monte Carlo).

Models & analysis

n/a	Involved in the study
☐	☐ Functional and/or effective connectivity
☐	☐ Graph analysis
☐	☐ Multivariate modeling or predictive analysis

Functional and/or effective connectivity	*Report the measures of dependence used and the model details (e.g. Pearson correlation, partial correlation, mutual information).*
Graph analysis	*Report the dependent variable and connectivity measure, specifying weighted graph or binarized graph, subject- or group-level, and the global and/or node summaries used (e.g. clustering coefficient, efficiency, etc.).*
Multivariate modeling and predictive analysis	*Specify independent variables, features extraction and dimension reduction, model, training and evaluation metrics.*